# Exploiting Symmetry in the Production and Measurement of Photon Pairs

**Rebecca Saaltink**

A thesis submitted to the
Faculty of Graduate and Postdoctoral Studies
in partial fulfilment of the requirements for the
MSc degree in Physics

Under the supervision of
Dr. Jeff S. Lundeen

Department of Physics
Faculty of Science
University of Ottawa

## Abstract

We present two projects that exploit symmetry to produce and measure photon pairs. The first project exploits the symmetry of nonlinear optical processes, while the second exploits the symmetry of quantum states. In the first of these two projects, we propose a method for directly producing radially and azimuthally polarized photon pairs through spontaneous parametric downconversion (SPDC). This method constitutes a novel geometry for SPDC in which a radially polarized Bessel-Gauss pump beam is directed into a nonlinear crystal, with the central propagation direction parallel to the crystal axis. The phasematching conditions are controlled by changing the opening angle of the pump beam; as the crystal axis cannot be tuned, we refer to this process as *super-critical phasematching*. We model and plot the spatial and polarization distributions for Type-I and Type-II phasematching.

In the second project, we demonstrate experimentally a method to measure the polarization state of single photons through direct measurements performed on optimal quantum clones. We produce these optimal quantum clones on a non-polarizing beam splitter by sending one photon with a target polarization state, and one photon in a maximally mixed state, into opposite ports of the beam splitter. We interfere the outputs of this beam splitter in a displaced Sagnac interferometer. By performing orthogonal polarization measurements on these two photons, we reconstruct the density matrix for target states $|H\rangle$ and $|R\rangle$.

# Exploiting Symmetry in the Production and Measurement of Photon Pairs

# 1 Summary

This thesis encompasses two projects that exploit the symmetry of quantum systems for measurement and photon pair production.

The first of these two projects explores a novel geometry for spontaneous parametric downconversion that produces photon pairs with cylindrical polarization symmetry. For this geometry, the pump beam is a radially polarized Bessel-Gauss beam that is directed into a uniaxial crystal with the central propagation axis of the beam in line with the optic axis of the crystal. The photon pairs produced by this method have azimuthal and radial polarizations. These two polarizations are mutually orthogonal, and due to their cylindrical symmetry they are rotationally invariant, which makes them well-suited for applications in quantum information, such as alignment-free quantum key distribution, single photon-spin orbit non-separable states, superdense coding, and quantum communication.

We begin by fully describing the proposed geometry to satisfy these phasematching conditions. Then, we give our simulation results showing the output probability distributions for these two downconverted photons. We then present a geometric argument for these output distributions, and discuss the correlations between the two photons. We also present a discussion on the feasibility of experimental realization of this phasematching geometry.

The second project exploits polarization symmetry in a different way. In this experiment, we measured the polarization state of single photons by making direct measurements on optimal quantum clones. These optimal quantum cones are produced on a non-polarizing beam splitter, by sending in a target state and a mixed state to opposite beam splitter ports. When the cloning is successful, the two photons are projected onto the symmetric subspace, i.e. the two photons exit the same port of the beam splitter. The density matrix that describes the polarization state of the target photon can be reconstructed by making orthogonal polarization measurements on the two photons when these photons are projected onto the symmetric subspace (exit the same port of the beam splitter), projected onto the anti-symmetric subspace (exit opposite ports of the beam splitter), and when these two cases are interfered using a $\sqrt{\text{SWAP}}$ gate, i.e. an interferometer with a phase of $\pm\pi/2$.

We begin with a discussion of measurement uncertainty and an overview of previous work to motivate this project. We demonstrate theoretically that the proposed experimental design gives the desired measurement outcomes by simulating, in Maple, the propagation of photon pairs through

the interferometer. We then demonstrate experimentally, through quantum state tomography, that the clones produced on this beam splitter are optimal, and that the polarization state of the clones closely matches that predicted by theory. For the second set of measurements, we show that the interferometer gives a phase of $\pi/2$ required to perform a $\sqrt{\text{SWAP}}$ operation. Finally, we perform orthogonal polarization measurements on the four configurations (symmetric, anti-symmetric, and $\sqrt{\text{SWAP}}$ with $\pm\pi/2$ phase) for target states $|H\rangle$ and $|R\rangle$, and demonstrate that the reconstructed density matrices match closely with the density matrices describing these target polarization states.

## 2 Contribution of Author and Acknowledgements

This thesis represents the work of many scientists in the quantum photonics research group at the University of Ottawa.

The novel geometry for SPDC that is proposed in Part I was proposed by Ebrahim Karimi, and was developed in collaboration with Robert Boyd and Lambert Giner. Under the guidance of my supervisor, Jeff Lundeen, I wrote the code that was used to simulate the output probability distributions for the two photons produced in this phasematching geometry. These simulations build on the work of Alan Migdall et. al. at NIST, who calculated characteristics of phasematching for the standard SPDC geometry. I adapted these phasematching calculations to our new, cylindrically symmetric geometry.

The experiment in Part II builds on the theoretical work of Holger Hofmann, who showed that the joint probabilities obtained from weak measurement also appear in correlations between cloned quantum systems. Jeff Lundeen proposed that these quantum clones could be used to measure the state of a quantum system directly. I was responsible for testing this proposal theoretically (using code written by Terry Rudolph) to confirm that the desired results could be obtained using our experimental design. I also designed, built, and tested the experimental setup, with assistance from Lambert Giner, Guillaume Thekkadath, Alec Fraser, and Tai Leung. I was responsible for the initial testing of this setup, including maximizing the photon pair production, construction and testing of the interferometer, and initial measurements of the optimal quantum clones. The data in Chapters 5.2.1 - 5.3.2 was collected by Guillaume Thekkadath, who has continued work on this project following the completion of this thesis.

# Part I
# Super-Critical Phasematching for Photon Pair Generation in Structured Light Modes

## 1 Introduction

Beams displaying radial and azimuthal polarizations have drawn great interest for their unique properties and uses in applied and fundamental optics. Radially polarized light beams have polarizations aligned radially toward the beam propagation axis. They produce a strong longitudinal electric field with a focal spot below the diffraction limit under tight focusing [1], [2]. Azimuthally polarized beams have polarizations at all points orthogonal to the beam radius. When focused, they produce a strong longitudinal magnetic field [3]. These two polarization modes are mutually orthogonal and display cylindrical symmetry about the beam axis. Radially and azimuthally polarized photons have gained increased interest in the quantum regime for applications in quantum information, such as alignment-free quantum key distribution (QKD) [4], [5], single photon spin-orbit non-separable states [6], superdense coding and quantum communication [7], as well as in the classical regime in optical data storage and optical lithography. When used along with standard $TEM_{00}$ modes in mode-division multiplexing they have been shown to increase the bandwidth of telecommunications channels [8], [9].

For propagation in free space, radially and azimuthally polarized Bessel-Gauss beams are solutions to the vectorial form of the paraxial wave equation [10]. These beams have a transverse profile given by the Bessel function of the first kind, $J_1$, multiplied by a Gaussian factor, since ideal Bessel beams are not physically achievable. They are desirable in optical applications because they exhibit non-diffracting propagation with an improved depth of focus over Gaussian beams [11], [12]. It is key to our modeling that a Bessel-Gauss beam can be decomposed into a distribution of Gaussian spatial mode beams with their central wave-vectors along the surface of a cone [13].

We are interested in producing radially and azimuthally polarized photon pairs through spontaneous parametric downconversion (SPDC). This is an optical process that occurs within a $\chi^{(2)}$ nonlinear crystal, in which one pump photon spontaneously decays to produce two photons at lower fre-

quencies. These two photons, commonly referred to as signal and idler, are correlated in position and momentum, and time and energy due to momentum-energy conservation [14]. Conservation of energy dictates that the frequencies of the two downconverted photons must add up to the pump frequency:

$$\omega_p = \omega_s + \omega_i. \tag{1}$$

Here, $\omega_p$, $\omega_s$, and $\omega_i$ are the frequencies of the pump, signal, and idler photons, respectively. In this paper we will restrict our attention to a CW pump laser, i.e. in effect, a single frequency. Downconverted photons may be produced with some $\mathbf{k}$-vector mismatch $\Delta\mathbf{k}$:

$$\mathbf{k}_s + \mathbf{k}_i - \mathbf{k}_p = \Delta\mathbf{k}. \tag{2}$$

Here, $\mathbf{k}_p$, $\mathbf{k}_s$, and $\mathbf{k}_i$ are any set of pump, signal, and idler $\mathbf{k}$-vectors. When $\Delta\mathbf{k}$ is zero, we have perfect phasematching, i.e. momentum conservation. Conditions (1) and (2) can be difficult to meet simultaneously because the $\mathbf{k}$-vectors of the pump, signal, and idler are related not only to the frequencies of each photon, but also to the indices of refraction within the nonlinear crystal, that is:

$$|\mathbf{k}_p| = \frac{2\pi n(\omega_p)}{\omega_p} \quad |\mathbf{k}_s| = \frac{2\pi n(\omega_s)}{\omega_s} \quad |\mathbf{k}_i| = \frac{2\pi n(\omega_i)}{\omega_i}. \tag{3}$$

To meet these two conditions simultaneously, this phasematching is performed in a birefringent crystal. Birefringent materials have indices of refraction that depend on the polarization of the incident light. Here, we consider a uniaxial birefringent crystal, which means that the anisotropy of the crystal may be described by a single axis, commonly referred to as the optic axis. Light entering along the optic axis will not experience any birefringence, but as the angle between the incident light and the optic axis increases, there is a difference in the indices of refraction experienced by orthogonal polarization components of the incident light. By selecting a particular set of polarizations for the pump, signal, and idler photons, the indices of refraction for these three photons can be set such that conditions (1) and (2) are met simultaneously.

In this paper, we focus on Type-II phasematching (a discussion on Type-I phasematching can be found in Appendix A). In Type-II phasematching, the pump beam has extraordinary polarization, that is, the polarization of the pump beam is in the plane formed b the crystal axis and the central pump $\mathbf{k}$-vector, $\mathbf{k}_p^0$. For Type-II phasematching, the signal and idler polarizations are

orthogonal. One of the downconverted photons has the same (extraordinary) polarization as the pump. The second downconverted photon is produced with a polarization that is perpendicular to the plan formed by the crystal axis and central pump **k**-vector. This is known as ordinary polarization. The downconverted photons may be emitted in different directions or, in the case of collinear downconversion, in the same direction. The wavelengths and emission directions of these photons depend on the angle of the pump beam relative to the optic axis of the crystal, and are constrained by the conservation rules given above in Eqs. (1) and (2). In the opposite process, sum-frequency generation, the amount of light produced is critically sensitive to the angle of the crystal. Hence, this type of phasematching is called *critical phasematching*.

We propose a novel geometry for SPDC that will produce photon pairs with one radially polarized and one azimuthally polarized photon. The pump is a radially polarized Bessel-Gauss beam that is focused into the crystal such that its cone axis is parallel to the crystal optic axis. The opening angle of the pump cone is chosen such that the central **k**-vector of each Gaussian beam in the pump distribution satisfies the phasematching conditions in Eq. (2). In this geometry, phasematching is achieved by adjusting the pump cone angle or, if possible, the crystal temperature. Since even the crystal angle cannot be adjusted anymore, we refer to this process as *super-critical phasematching*. In this paper, we model the spatial and polarization properties of the generated photon pairs.

## 2 Geometry and Notaton

In this section, we fully describe the proposed geometry for super-critical phasematching. We define the crystallographic axes by $\mathbf{x}$, $\mathbf{y}$, and $\mathbf{z}$, as shown in Fig. 1, where $\mathbf{z}$ is the optic axis (we restrict our analysis to a uniaxial crystal). We consider degenerate phasematching, i.e. the signal and idler wavelengths are the same.

As mentioned in the introduction, a Bessel-Gauss pump beam, BG($\mathbf{k}$), can be thought of as a distribution of Gaussian beams around a cone [13]:

$$BG(\mathbf{k}) \propto \int_0^{2\pi} e^{-w_p^2(\mathbf{k}-\mathbf{k}_p^0(\varphi_p))^2/4} d\varphi_p, \tag{4}$$

$$\begin{aligned} k_{p,x}^0(\varphi_p) &= |\mathbf{k}_p^0| \sin(\theta_p)\cos(\varphi_p), \\ k_{p,y}^0(\varphi_p) &= |\mathbf{k}_p^0| \sin(\theta_p)\sin(\varphi_p), \\ k_{p,z}^0 &= |\mathbf{k}_p^0| \cos(\theta_p) \end{aligned}$$

where each of these Gaussian beams has a central $\mathbf{k}$-vector given by $\mathbf{k}_p^0(\varphi_p)$ (with components $k_{p,j}^0$ for $j = x, y, z$) , $w_p$ is the $1/e^2$ spatial full-width of the pump beam, $\theta_p$ is the opening half-angle of the cone, and $\varphi_{s(i)}$ is the azimuthal angle. Thus, the cone axis is parallel to the $z$-axis the crystal. Decomposing the Bessel-Gauss beam into this distribution has the advantage that each Gaussian beam may be treated in the paraxial approximation, whereas the full Bessel-Gauss beam can be non-paraxial if the cone angle is large. We use a proportionality symbol in Eq. (4) and later in the paper since we will impose an overall normalization later.

The $\mathbf{k}$-vectors of the signal and idler photons are denoted by $\mathbf{k}_s$ and $\mathbf{k}_i$, respectively. The emission directions of these photons are characterized by two angles, $\theta_{s(i)}$ and $\varphi_{s(i)}$, of spherical coordinates. The first, $\theta_{s(i)}$, is measured between the $\mathbf{k}$-vector of the signal(idler) photon and the $z$-axis of the crystal. The azimuthal angle, $\varphi_{s(i)}$, represents a rotation from the $x$-axis in the transverse plane of the crystal. The angles of the pump, signal, and idler photons are defined in the crystal frame of reference, that is, with respect to $\mathbf{x}$, $\mathbf{y}$, and $\mathbf{z}$. These angles are shown in Fig. 1.

We also define a rotated local frame given by $\mathbf{x}'$, $\mathbf{y}'$ and $\mathbf{z}'$. Here, local means that the axes are defined with respect to the central pump $\mathbf{k}$-vector $\mathbf{k}_p^0$ of a Gaussian beam in our distribution in Eq. (4), such that $\mathbf{z}'$ is in the same direction as $\mathbf{k}_p^0$. The $\mathbf{y}'$ axis is in the plane of $\mathbf{z}$ and $\mathbf{z}$'. The $\mathbf{x}'$ axis is perpendicular to this plane. Consequently, the local frame rotates in the integral in Eq. (4). That is, for every value of the integrand the axes are

aligned azimuthally ($\mathbf{x}'$) and radially ($\mathbf{y}'$) with respect to $\mathbf{z}$. Conversely, the axes $\mathbf{x}$, $\mathbf{y}$, $\mathbf{z}$ are stationary with respect to the crystal, as they are defined with respect to the optic axis of the crystal. The coordinate transformations between $\mathbf{x}$, $\mathbf{y}$, $\mathbf{z}$ and $\mathbf{x}'$, $\mathbf{y}'$, $\mathbf{z}'$ are given in Eq. (17) from Appendix B, and are from Ref. [15].

As an example, we consider a negative uniaxial crystal (e.g. $\beta$-barium borate (BBO)) in which the only phasematched process occurs for an extraordinarily (e) polarized pump beam. Extraordinary polarization is defined to be in the plane formed by a beam's wavevector $\mathbf{k}$ and the crystal optic axis $\mathbf{z}$, whereas ordinary (o) polarization is orthogonal to this plane. In terms of our local frame, the pump polarization is along $\mathbf{y}'$. As $\mathbf{y}'$ is aligned radially with respect to $\mathbf{z}$, the extraordinary polarized Gaussian beams in the pump distribution in Eq. (4) form a Bessel-Gauss beam that is radially polarized.

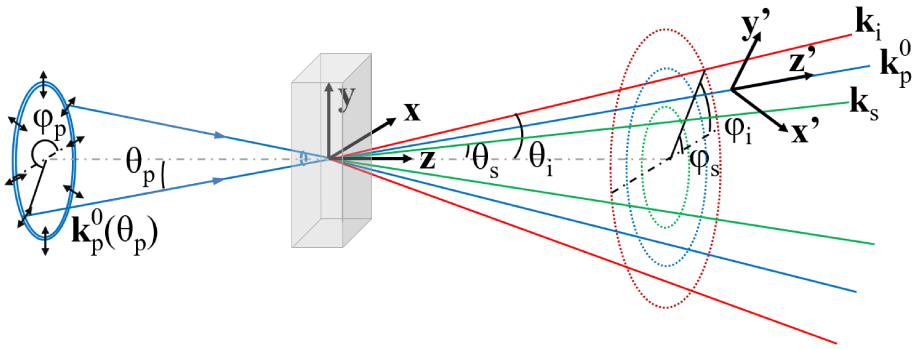


*Figure 1: The geometry of super-critical phasematching. The* $\mathbf{x}$, $\mathbf{y}$, *and* $\mathbf{z}$ *axes are the crystallographic axes, where* $\mathbf{z}$ *is the optic axis. The pump (blue) is comprised of a conical distribution of Gaussian beams, each with central* $\mathbf{k}$*-vector* $\mathbf{k}_p^0(\varphi_p)$*, where* $\varphi_p$ *is the azimuthal angle. The pump beam cone axis is along the crystal axis* $\mathbf{z}$*, and the opening half-angle of the cone is* $\theta_p$*. The signal (idler), shown in green (red), is emitted with* $\mathbf{k}$*-vector* $\mathbf{k}_{s(i)}$*. The signal (idler)* $\mathbf{k}$*-vector is characterized by two angles:* $\theta_{s(i)}$*, the half-cone opening angle, measured between the signal (idler)* $\mathbf{k}$*-vector and the* $\mathbf{z}$ *axis; and* $\varphi_{s(i)}$*, the azimuthal angle. We also introduce a local frame, denoted by* $\mathbf{x}$*'*, $\mathbf{y}$*'*, *and* $\mathbf{z}$*'*, *where* $\mathbf{z}$*' is defined along the central* $\mathbf{k}$*-vector,* $\mathbf{k}_p^0$*, of each Gaussian beam. The other axes are aligned azimuthally (*$\mathbf{x}$*') and radially (*$\mathbf{y}$*') with respect to* $\mathbf{z}$*.*

## 3 Simulation Results

We give a brief description of our methods here; a full description of our calculations can be found in Appendix B. In this section, we simulate the output **k**-vector distributions of the downconverted photons for a super-critically phasematched Bessel-Gauss pump beam. This type of beam can be strongly non-paraxial, which means standard methods for modeling the output distribution can be difficult to apply. Instead, we begin by modelling the output from a single Gaussian pump centered on $\mathbf{k}_p^0(\varphi_p)$. That is, we model the complex amplitude $\Phi_G(\mathbf{k}_p^0(\varphi_p), \mathbf{k}_s, \mathbf{k}_i)$ for the signal and idler photons to have wavevectors $\mathbf{k}_s$ and $\mathbf{k}_i$. Then we superpose these amplitudes similar to in Eq. (4) to find the total complex amplitude output from a Bessel-Gauss pump:

$$\Phi_{BG}(\mathbf{k}_s, \mathbf{k}_i) = \frac{1}{\sqrt{N}} \int_0^{2\pi} \Phi_G(\mathbf{k}_p^0(\varphi_p), \mathbf{k}_s, \mathbf{k}_i) d\varphi_p, \tag{5}$$

The scaling,$\sqrt{N}$ ensures that the joint probability distribution $|\Phi_{BG}|^2$ is normalized. In [15], Boeuf et al. demonstrate that the complex amplitude $\Phi_G$ can be expressed as:

$$\Phi_G(\mathbf{k}_p^0(\varphi_p), \mathbf{k}_s, \mathbf{k}_i) \propto \exp\left(\frac{-w_p^2(\Delta k_{x'}^2 + \Delta k_{y'}^2)}{4}\right) \operatorname{sinc}\left(\frac{L_{optic}\Delta k_{z'}}{2}\right) \exp\left(\frac{iL_{optic}\Delta k_{z'}}{2}\right), \tag{6}$$

in which $\Delta k_{x'}$, $\Delta k_{y'}$, and $\Delta k_{z'}$ (given in Appendix A2) are the **k**-vector mismatches in the $\mathbf{x}'$, $\mathbf{y}'$, and $\mathbf{z}'$ directions. Here, $L_{\text{optic}}$ is the length of the optical path through the crystal. That is, $L_{\text{optic}} = L_{\text{crystal}}/\cos(\theta_p)$, where $L_{\text{crystal}}$ is the crystal length as measured along its normal.

Equation (6)gives the amplitude to produce signal and idler photons at $\mathbf{k}_s$ and $\mathbf{k}_i$, respectively, for a Gaussian pump beam with central **k**-vector $\mathbf{k}_p^0$. The first exponential term and sinc term give the square root of the phasematching function from [15]. The first exponential term gives the amplitude for transverse phasematching, that is, in the $x'$- and $y'$-directions. A small **k**-vector mismatch in the transverse directions may still lead to phasematching because of the finite width of the pump (i.e. the pump has some small spread of **k**-vectors centered on $\mathbf{k}_p^0$). The second term gives the amplitude for phasematching in the longitudinal direction, that is, along the $z'$-direction. The second exponential term gives the phase.

The phasemathing equation in [15] is obtained by taking the Hamiltonian interaction integral for this process. For an infinitely long crystal and an

infinitely wide pump beam, this integral is taken over all space, and the interaction yields a delta function:

$$\int\int\int \exp\left(i \cdot \Delta\mathbf{k}\right) d^3r \propto \delta\left(\Delta\mathbf{k}\right). \tag{7}$$

This equation will give 0 for all cases except when there is perfect phasematching, i.e. when $\Delta\mathbf{k} = 0$. For a finite crystal length, L, and finite pump width $w_p$, this integral gives $|\Phi_G|^2$, which is the phasematching equation in [15]. For our calulations, we take $\Phi_G$ instead of $|\Phi_G|^2$ because a signal (idler) produced at $\mathbf{k}_{s(i)}$ may have come from one of several beams in the pump distribution. It is then necessary to sum the amplitudes from each of these Gaussian pump beams before taking $|\Phi_G|^2$.

In our simulations, the pump cone half-angle $\theta_p$ is set to 41.8° inside a 500 $\mu m$ thick BBO crystal. This crystal thickness ensures that the sinc width in Eq. (6) is sufficiently large to capture in a numerical simulation, and the angle, $\theta_p$, is the angle for Type-II degenerate collinear phasematching at 405 nm for a typical SPDC geometry. This value of the pump angle corresponds to the typical angle used to produce photons within the sensitivity range of silicon detectors while still having a pump at a typical laser wavelength. More specifically, with a pump wavelength at 405 nm and in the case of degenerate SPDC, the signal and idler wavelengths are 810 nm. All of these parameters are typical in an SPDC experiment. Thus, every Gaussian beam in the pump distribution satisfies phasematching conditions within the BBO crystal. Each Gaussian pump beam has a $1/e^2$ spatial full-width of 84 $\mu$m. We have made the assumption that the pump, signal, and idler photons are each at a single wavelength, which is reasonable if the pump beam has a sufficiently narrow bandwidth.

Rather than plotting the joint probability density $|\Phi_{BG}(\mathbf{k}_s, \mathbf{k}_i)|^2$ for signal and idler, which is made difficult by computation power limitations, we plot the marginal probability distribution for the signal *or* idler photon. For example, we plot $P(\mathbf{k}_s) = \int\int |\Phi_{BG}|^2 dk_{i,x} dk_{i,y}$ . The results are shown in Fig. 2 and are given in the crystal frame ($\mathbf{x}$, $\mathbf{y}$, $\mathbf{z}$). Since for degenerate phasematching $|\mathbf{k}_{s(i)}|$ is fixed, $\mathbf{k}_{s(i),x}$ and $\mathbf{k}_{s(i),y}$ (or, equivalently, $\theta_{s(i)}$ and $\varphi_{s(i)}$) completely determine the signal and idler wavevectors, so these plots are produced with respect to $\mathbf{k}_{s(i),x}$ and $\mathbf{k}_{s(i),y}$ only. The resulting output distribution shows three concentric circles which we call "supercones" (for reasons that will be apparent later). Signal photons are produced along the innermost and central supercones, and idler photons are produced along the central and outermost supercones.

Implicit in our calculations are the polarization properties of the signal

and idler photons. In Type-II phasematching, one downconverted photon (signal) is extraordinarily polarized and the other photon (idler) is ordinarily polarized. Thus for each $\mathbf{k}_p^0(\varphi_p)$ in Eq. (5) the signal is polarized along $\mathbf{y}'$ and the idler is polarized along $\mathbf{x}'$. It follows that the signal output supercones are polarized radially and the idler output supercones are polarized azimuthally with respect to the $\mathbf{z}$-axis.

At this point, we do not include the effect of refraction at the input or output crystal face. If the the input and and output faces are perpendicular to the $\mathbf{z}$-axis then Snell's law would imply that the opening angles $\theta$ in free space outside the crystal will be greater than those inside. The overall shape of the distributions shown in Fig. 2 would be retained, but refraction would increase the radii of the rings. This refraction will need to be taken into account for the experimental realization of this work. Furthermore, since the phasematching angle is chosen to produce signal and idler collinear with the pump, the high incidence angle at the crystal output face would cause the signal and idler to be separated in angle by 2.9°, which would cause them to spatially separate as they propagate. However, this is simple to precompensate by changing the phasematching angle so that they are generated within the crystal with a 2.9° angle separation. Propagating across the crystal, this itself would cause a spatial walkoff. But, this effect is small compared to the pump full width and can, thus, be neglected. These concerns are addressed further in Section 6.

In summary, by pumping with a Bessel-Gauss beam parallel to the crystal's optical axis one can generate radially and azimuthally polarized photon pairs in cylindrically symmetric spatial modes. It is important to note, these supercones are not the cone-like output distributions normally associated with critically phasematched SPDC. Namely, the supercones are cylindrically symmetric about the crystal's optical axis $\mathbf{z}$, whereas the latter are centered on the pump axis $\mathbf{z}'$. However, to understand how these supercones come about, in the next section we start by considering the typical output distributions for critically phasematched SPDC.

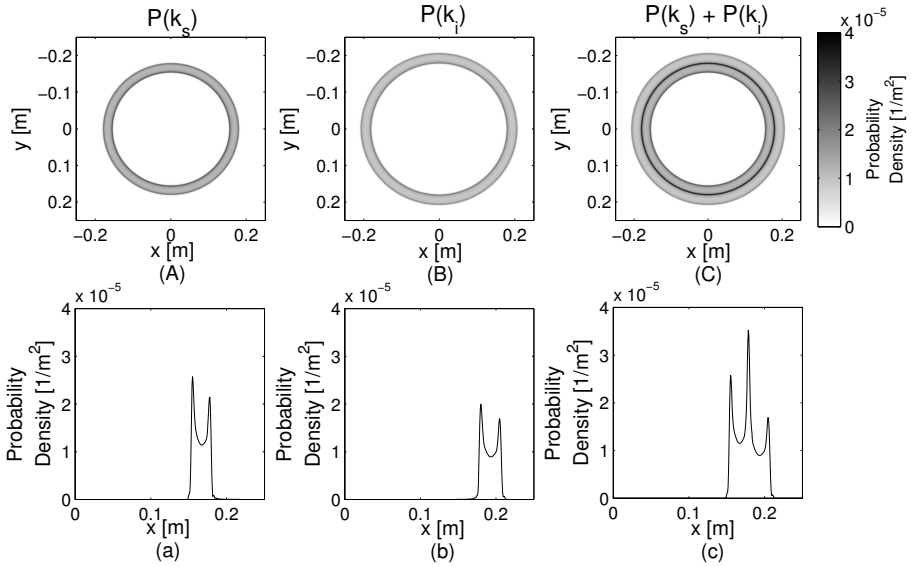


*Figure 2: Marginal probability density ($P(\boldsymbol{k}_s)$, $P(\boldsymbol{k}_i)$) for Type II degenerate down-conversion. The pump cone half-angle is* $41.8°$ *in a* $500$ *$\mu$m-thick BBO crystal. The pump beam wavelength is 405 nm and the signal and idler wavelengths are 810 nm. Plots (A), (B), and (C) give (A) the probability density of generating a signal photon at* $\mathbf{k}_s$*, (B) the probability density of generating an idler photon at* $\mathbf{k}_i$*, and (c)* $P(\mathbf{k}_s) + P(\mathbf{k}_i)$*, which is proportional to the photon flux. Plots (a), (b), and (c) are produced from plots (A), (B), and (C), respectively, by plotting along* $y = 0$*.*

# 4 Expected Output

In this section, we give a geometric argument for the spatial distributions for the signal and idler photons shown in Fig. 2. We do this by considering Type-II critical phasematching of a single Gaussian beam in the pump distribution in Eq. (4). By considering only a single Gaussian pump we revert to the standard geometry for SPDC, in which the pump beam travels at an angle $\theta_p$ to the crystal's optical axis.

The phasematching conditions for this Gaussian pump beam may be met by a range of signal and idler emission angles. In the simulation, we considered the case where $\theta_p$ is set to $41.8°$. For degenerate SPDC with a 405 nm pump this produces an idler and signal output cone at 810 nm, each meeting tangentially at the pump $\mathbf{k}$-vector, $\mathbf{k}_p^0$ . We call these the standard Type-II cones.

If we consider one such Gaussian pump beam, labelled by its central $\mathbf{k}$-vector $\mathbf{k}_p^0$ in Fig. 3-(a), then the signal and idler photons produced by this

Gaussian beam will be generated along the standard Type-II cones, shown in Fig.3-(b). We can then take this standard Type-II SPDC output and apply the superposition principle to arrive at the expected output distribution for a Bessel-Gauss pump. In more detail, this output can be visualized by taking the two standard Type-II cones and rotating them around the crystal optical axis (**z**-axis), as illustrated in Fig. 3-(c). Rotation of the idler standard cone results in two larger and concentric cones, now centered on the $z$-axis. These are the supercones we observe in Fig. 2. Similar supercones are produced by the rotation of the signal standard cone, one with the same diameter as the inner idler supercone and the other with a smaller diameter. Photon pairs may be produced in the regions between these supercones, but with lower probability, as can be seen in the profiles in Fig. 2.

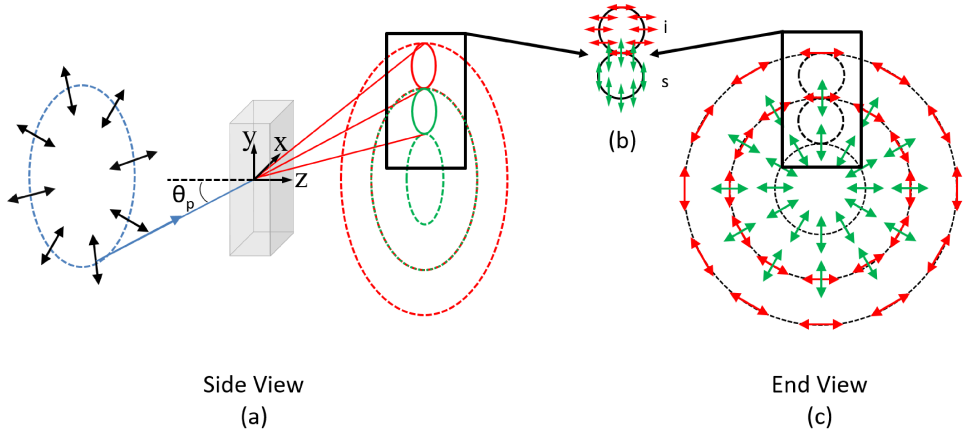


*Figure 3: Spatial (a) and polarization (c) distributions for degenerate Type-II supercritical phasematching. The polaization distribution in (b) is the typical distibution for a Gaussian pump beam. When this output is summed for all Gaussian beams in the Bessel-Gauss pump distribution in Eq. (4), the resulting intensity and polaization distributions become those in (a) and (c). The signal photons (green) are generated with radial polarizations and the idler photons (red) are generated with azimuthal polarizations.*

In this section, we have shown that the supercones seen in the simulation results have an intuitive geometric origin that can be understood by considering the standard output distributions for Type-II phasematched SPDC. Here, we only discussed as an example the case in which $\theta_p$ is set to 41.8°. Different pump cone half-angles will change the diameter and intersection of the standard Type-II SPDC output circles. Using our intuitive geometric argument, one would expect more supercones to appear, two for each

standard cone.

Up to this point, we have only discussed the signal and idler marginal probability densities. In the next section, we examine the signal and idler joint probability density.

# 5 Correlations

One method to determine the correlations between the signal and idler photons is to calculate the full 4d (i.e. $k_{s,x}$, $k_{s,y}$, $k_{i,x}$, $k_{i,y}$) signal and idler probability density $|\Phi_{BG}(\mathbf{k}_s, \mathbf{k}_i)|^2$. This would be achieved by calculating the phasematching amplitude in Eq. (5) using 4d matrices of $\varphi_s$, $\theta_s$, $\varphi_i$, $\theta_i$ to give the phasematching amplitude for all possible combinations of these emission angles for the signal and idler. However, this calculation would be prohibitively large, so we instead simulate the probability density for the signal photon given the idler photon has a particular transverse wavector $\mathbf{k}_{i,T} = |\mathbf{k}_i|(\widehat{\mathbf{x}}+\widehat{\mathbf{y}})/\sqrt{2}$ (where $\widehat{\mathbf{x}}$ and $\widehat{\mathbf{y}}$ refer to unit vectors along the x and y axis). We limit our discussion to the overlapping signal and idler supercone. That is, $k_{i,x}$ is chosen to be at the peak probability of this supercone. The results are shown in Fig. 4.

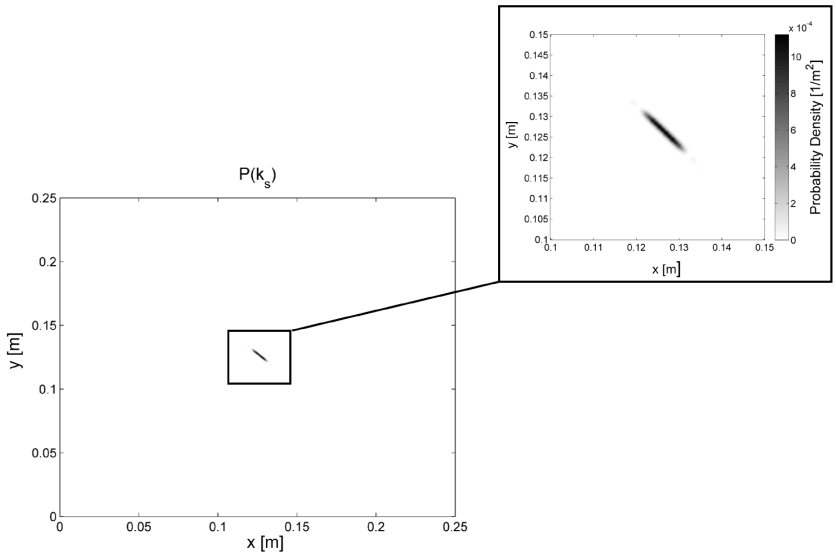


*Figure 4: Signal photon probability density for Type II degenerate collinear down-conversion with a fixed idler emission direction. Idler angles are fixed at $\theta_i = 41.8°$ and $\varphi_i = 45°$.*

The resulting signal conditional probability density has a FWHM width of 7.9 mm in the $y'$ direction (azimuthal), which is 1.3% of the circumference of the signal supercone. In the $x$' direction (radial), the conditional probability density has a width of 2.7 mm, which is 39% of the supercone FWHM thickness. Switching the role of signal and idler, these parameters are the

same. It is evident that signal and idler emission directions are strongly correlated: $\mathbf{k}_s$ eqals $\mathbf{k}_i$ to within the phasematching uncertainty set by Eq. (6). Both photons appear in the same spot in the overlapping supercone.

The strong correlations in the simulation imply that the full signal-idler two-photon wavefunction is highly entangled in both polarization and in spatial mode. In this situation the position of, say, the idler photon reveals the position of the signal. In quantum mechanics, the presence of this "which-position" information requires absence of coherence between positions. Consequently, one cannot consider each photon, by itself, to be in a Bessel-Gauss quantum state, which would require coherence across the supercone. In particular, focusing the idler or signal photon supercone will result in a much broader distribution than what one would expect from a Bessel-Gauss mode of this diameter. This is despite the fact that the marginal probability densities (Fig. 2) and polarizations (Fig. 3) of the signal and idler appear similar to those of radially and azimuthally polarized Bessel-Gauss modes, respectively.

On the other hand, applications in quantum information rely on entanglement and also on the symmetry of the overall two-photon state. This is why we expect the highly-entangled cylindrically symmetric two-photon states that this geometry produces to have many uses in this area.

## 6 Feasibility of Experimental Realization

The construction of a super-critically phasematched SPDC source will require consideration of refraction at the crystal face. While the axis of the pump cone is perpendicular to the crystal face, its opening angle, and hence its incidence angle, can be large. For the scenario discussed above, the opening half-angle of the pump cone is $\theta_p = 41.8°$ inside the crystal. This is larger than the angle of total internal reflection for BBO, which is 38° at 405 nm. To circumvent this problem, we suggest two means of reducing the angle of the pump beam relative to the crystal face.

The first of these is to cut each face of the crystal as an axicon. That is, the crystal would be a double-sided cone with an apex full-angle of 90°. This reduces the pump beam angle to 5.1° relative to the surface of the crystal, as shown in Fig. 5. However, the pump angle is still quite large, 39.9° relative to the $z$-axis, so another 90° axicon is required to direct a diverging Bessel-Gauss pump beam (opening angle 3°) into the crystal. The pump beam is focused into the crystal when it passes through this axicon. An axicon is also placed at the exit face of the crystal to reduce the angle of the emitted cones of pump, signal, and idler photons.

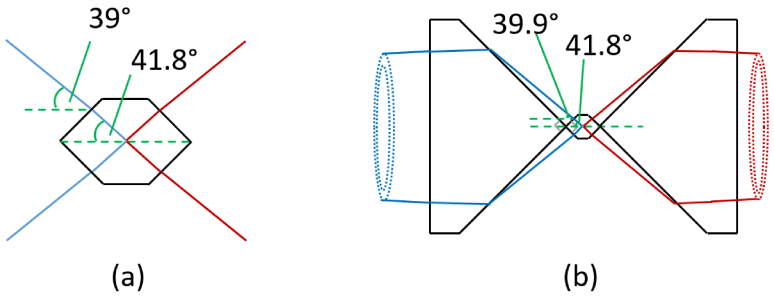


*Figure 5: Proposed setup to reduce the pump opening angle in air. Angles are calculated for Type-II degenerate SPDC from 405 nm to 810 nm. The pump beam angle is reduced by two means: (a) a crystal cut as a double-sided 90° axicon, and (b) two 90° axicons placed tip-to-tip with the crystal at the entry and exit faces. The pump beam is focused into the crystal as it passes through the first axicon. The second axicon reduces the angle of the output beams as they exit the crystal.*

However, this method is not ideal because the cut of the crystal is not conventional and may be difficult to fabricate. Another method is to reduce the phasematching angle, $\theta_p$, by performing Type-II downconversion at a longer pump wavelength. To achieve the same standard Type-II ge-

ometry as discussed in Section 2 but for SPDC from 775 nm to 1550 nm, the phasematching angle is $\theta_p = 28.7°$. This is less than the angle of total internal reflection for BBO, which avoids the need for an unusual crystal shape. However, due to refraction at the crystal face the pump beam must be focused into the crystal at an angle of 51.8° to meet phasematching conditions inside the crystal. This focusing angle is difficult to achieve, but can be reduced by affixing two 90° axicons back-to-back on either side of the crystal, as shown in Fig. 6. The index of glass is similar to that of BBO so the pump beam does not refract significantly when entering the crystal through the axicon. Thus, a pump beam that is focused at 25.7° relative to the horizontal is sufficient to produce an angle of 28.7° inside the crystal. The axicon affixed to the exit face of the crystal similarly reduces the exit angles of the pump, signal, and idler supercones.

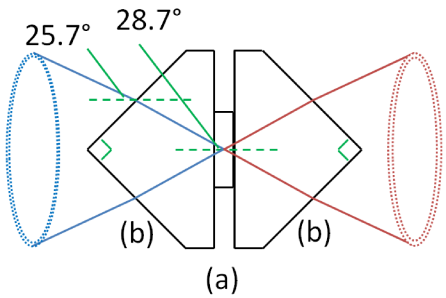


*Figure 6: Proposed setup to reduce the pump opening angle in air for Type-II degenerate SPDC from 775 nm to 1550 nm: (a) a BBO crystal, placed between (b) two* 90° *axicons, which are affixed back-to-back on either side of the crystal. The required opening angle of the pump in air is* 25.7°*; without the axicons at the crystal face this angle would be* 51.8°*.*

The use of periodically poled KTP was also considered as a means of reducing the entry angle into the crystal for Type-II phasematching. This would require that the crystal be poled with the optical axis parallel to the beam propagation axis; however, current poling methods only allow for the optical axis to be perpendicular to the direction of propagation. KTP is also biaxial, which means that the crystal principal indices of refraction in the $x$- and $y$- directions are not exactly equal at a given wavelength. As a result, the pump azimuthal angle $\varphi_p$ would affect the phasematching conditions and the cylindrical symmetry would be lost.

An additional experimental consideration is the polarization of the pump beam. Due to the difficulty in producing a radially polarized pump beam, it

may be advantageous to instead produce a circularly polarized Bessel-Gauss beam with an OAM value of $\pm 1$, the sign being opposite to the handedness of the polarization. This beam has equal azimuthal and radial polarization components. Only the radial component will contribute to the production of photon pairs because this is the extraordinary component of the pump beam. As a result, the contributing intensity will be half that of the total intensity.

# 7 Conclusion

We have described a novel, cylindrically symmetric geometry for spontaneous parametric downconversion with the aim of producing radially and azimuthally polarized photon pairs. The pump beam is a radially (or alternatively, circularly) polarized Bessel-Gauss beam, which can be thought of as a distribution of Gaussian beams with central **k**-vectors forming the surface of a cone. The pump beam is focused into a nonlinear crystal such that the cone axis is along the optical axis of the crystal.

We numerically simulated the output distributions of the signal and idler photons. The photons emerge along cylindrically symmetric (about the optical crystal axis) distributions which we call supercones. The signal photons will be emitted with radial polarizations and the idler photons will have azimuthal polarizations. The photons exhibit strong correlations such that the signal and idler appear in the same location in the central supercone. Consequently, the associated two-photon wavefunction is strongly entangled both in polarization and in spatial mode.

While not the focus of this paper, this beam geometry could potentially improve the efficiency of the reverse process, second harmonic generation (SHG), in which two photons combine to produce one photon at a higher frequency. As this requires the presence of two photons, the efficiency of SHG depends quadratically on the intensity of the beam. Focusing the beam more tightly to increase this intensity causes the beam to diffract more quickly, so the crystal length is limited by the Rayleigh range of the beam [16]. Bessel beams may provide improved conversion efficiencies over Gaussian beams due to their non-diffracting properties, in that they maintain a high peak intensity over larger distances [17]. Attempts have been made to experimentally test this idea. In particular, truncated Bessel beams were used to pump Type-I phasematching in lithium triborate [18]. In that paper, measured conversion efficiencies were slightly lower than those obtained for a Gaussian pump. However, that geometry consisted of an input beam traveling perpendicular to the crystal axis in *non-critical* phasematching, and showed only longitudinal or transverse phasematching, but not both concurrently. As this is significantly different from our *super-critical* phasematching, it is worth again considering whether Bessel beams can enhance SHG efficiency.

## References


[1] S. Quabis, R. Dorn, M. Eberler, O. Glockl, and G. Leuchs, "Focusing light to a tighter spot," *Opt. Commun.*, vol. 179, no. 1, pp. 1–7, 2000.

[2] R. Dorn, S. Quabis, and G. Leuchs, "Sharper focus for a radially polarized light beam," *Phys. Rev. Lett.*, vol. 91, no. 23, p. 233 901, 2003.

[3] H. Wang, L. Shi, B. Lukyanchuk, C. Sheppard, and C. T. Chong, "Creation of a needle of longitudinally polarized light in vacuum using binary optics," *Nat. Photonics*, vol. 2, no. 8, pp. 501–505, 2008.

[4] G. Vallone, V. D'Ambrosio, A. Sponselli, S. Slussarenko, L. Marrucci, F. Sciarrino, and P. Villoresi, "Free-space quantum key distribution by rotation-invariant twisted photons," *Phys. Rev. Lett.*, vol. 113, no. 6, p. 060 503, 2014.

[5] V. D'Ambrosio, E. Nagali, S. P. Walborn, L. Aolita, S. Slussarenko, L. Marrucci, and F. Sciarrino, "Complete experimental toolbox for alignment-free quantum communication," *Nature communications*, vol. 3, p. 961, 2012.

[6] E. Karimi, J. Leach, S. Slussarenko, B. Piccirillo, L. Marrucci, L. Chen, W. She, S. Franke-Arnold, M. J. Padgett, and E. Santamato, "Spin-orbit hybrid entanglement of photons and quantum contextuality," *Phys. Rev. A*, vol. 82, no. 2, p. 022 115, 2010.

[7] G. Milione, T. A. Nguyen, E. Karimi, D. A. Nolan, S. Slussarenko, L. Marrucci, and R. Alfano, "Superdense coding with vector vortex beams: A classical analogy of entanglement," in *Frontiers in Optics 2013*, Optical Society of America, 2013, FM3F.4.

[8] N. Bozinovic, Y. Yue, Y. Ren, M. Tur, P. Kristensen, H. Huang, A. E. Willner, and S. Ramachandran, "Terabit-scale orbital angular momentum mode division multiplexing in fibers," *Science*, vol. 340, no. 6140, pp. 1545–1548, 2013.

[9] G. Milione, M. P. J. Lavery, H. Huang, Y. Ren, G. Xie, T. A. Nguyen, E. Karimi, L. Marrucci, D. A. Nolan, R. R. Alfano, and A. E. Willner, "4x20 gbit/s mode division multiplexing over free space using vector modes and a q-plate mode (de)multiplexer," *Opt. Lett.*, vol. 40, no. 9, pp. 1980–1983, May 2015.

[10] R. H. Jordan and D. G. Hall, "Free-space azimuthal paraxial wave equation: The azimuthal bessel–gauss beam solution," *Opt. Lett.*, vol. 19, no. 7, pp. 427–429, Apr. 1994.

[11] D. McGloin and K. Dholakia, "Bessel beams: Diffraction in a new light," *Contemporary Physics*, vol. 46, no. 1, pp. 15–28, 2005.

[12] P. L. Greene and D. G. Hall, "Diffraction characteristics of the azimuthal bessel-gauss beam," *JOSA A*, vol. 13, no. 5, pp. 962–966, 1996.

[13] D. N. Schimpf, W. P. Putnam, M. D. Grogan, S. Ramachandran, and F. X. Kartner, "Radially polarized bessel-gauss beams: Decentered gaussian beam analysis and experimental verification," *Opt. Express*, vol. 21, no. 15, pp. 18 469–18 483, 2013.

[14] S. P. Walborn, C. Monken, S. Padua, and P. S. Ribeiro, "Spatial correlations in parametric down-conversion," *Phys. Rep.*, vol. 495, no. 4, pp. 87–139, 2010.

[15] N. Boeuf, D. Branning, I. Chaperot, E. Dauler, S. Gue, G. Jaeger, A. Muller, A. Migdall, *et al.*, "Calculating characteristics of noncollinear phase matching in uniaxial and biaxial crystals," *Opt. Eng.*, vol. 39, no. 4, pp. 1016–1024, 2000.

[16] G. D. Boyd and D. A. Kleinman, "Parametric interaction of focused gaussian light beams," *J Appl. Phys.*, vol. 39, no. 8, pp. 3597–3639, 1968.

[17] K. Shinozaki, C.-q. Xu, H. Sasaki, and T. Kamijoh, "A comparison of optical second-harmonic generation efficiency using bessel and gaussian beams in bulk crystals," *Opt. Commun.*, vol. 133, no. 1, pp. 300–304, 1997.

[18] J. Arlt, K. Dholakia, L. Allen, and M. J. Padgett, "Efficiency of second-harmonic generation with bessel beams," *Phys. Rev. A*, vol. 60, pp. 2438–2441, 3 Sep. 1999.

# Appendix A Type-I Downconversion

We consider here the case of Type-I degenerate phasematching. Fig. 8 shows the simulated probability densities $|\Phi_{BG}|^2$ for the signal and idler, where $\Phi_{BG}$ is defined as in Eq. (5). The pump opening half-angle $\theta_p$ was set to 28.8° inside the crystal. In the standard Type-I geometry, this is the phasematching angle that would produce signal and idler photons collinear with the pump beam. In contrast, for a Bessel-Gauss pump the resulting SPDC output distribution is a single supercone that is at all points collinear with the pump cone.

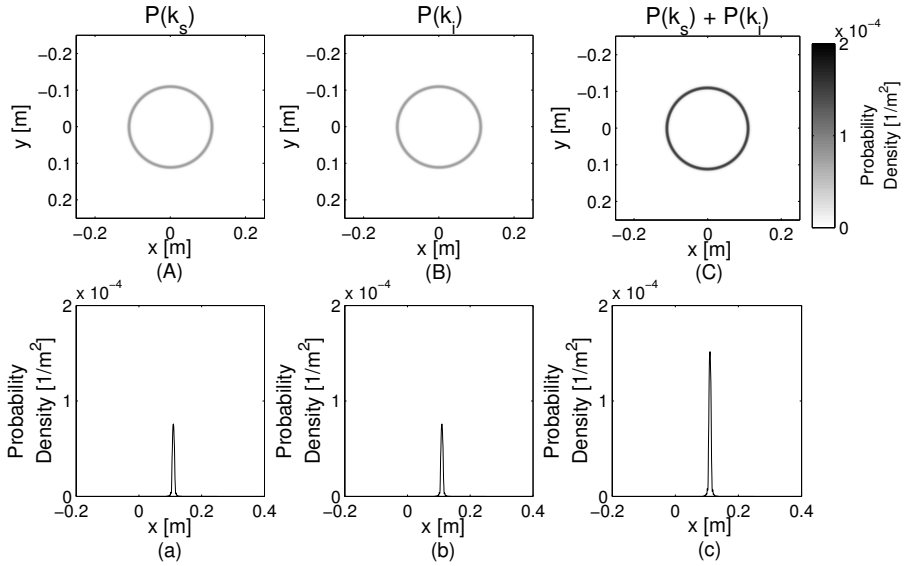


*Figure 7: Probability densities for Type-I degenerate downconversion in a 500 $\mu m$ -thick BBO crystal for a pump beam wavelength of 405 nm, and signal and idler wavelength of 810 nm. Plots (A), (B), and (C) give (A) the probability density for the signal photon, $P(\mathbf{k}_s)$; (B) the probability density for the idler photon, $P(\mathbf{k}_i)$; and (C) $P(\mathbf{k}_s) + P(\mathbf{k}_i)$, which is proportional to the photon flux. Plots (a), (b), and (c) are produced from plots (A), (B), (C), respectively, by plotting along $y = 0$.*

This output distribution can be understood by superposing the typical Type-I SPDC outputs for each Gaussian beam in the pump distribution in Eq. (5). Each of these Gaussian beams produces collinear signal and idler photons. Consequently, only one supercone is produced containing both signal and idler photons. For Type-I phasematching, the signal and idler are emitted with ordinary polarizations. When these outputs are superposed for all Gaussian beams in the pump distribution, the resulting polarization

distribution is azimuthal. This polarization distribution is shown in Fig. 8.

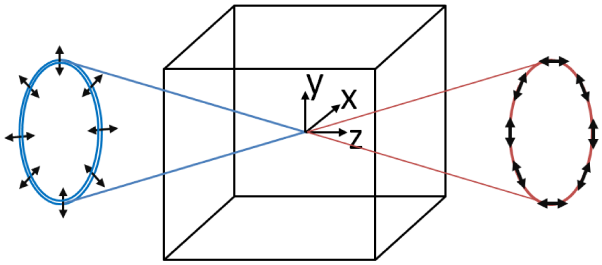


*Figure 8: Expected output for Type-I collinear downconversion with a conical pump beam centered on the optic axis (z). The signal and idler photons are produced in a single supercone centered on the optic axis.*

The Type-I phasematching angle is below the angle of total internal reflection for BBO at 405 nm; however, there is still significant refraction at the crystal face so a reduction in the free-space opening angle of the pump beam is required. The pump beam can be focused into the crystal using a similar setup as in Fig. 6.

## Appendix B Calculation of Output Distributions

The output distributions shown in Figs. 2 and 7 were calculated in Matlab and took 8 days to run on a core i5 processor. For most of the work below we follow the work of Ref. [1]. We start with a 750 by 750 grid in $x$ and $y$, with a range large enough to accommodate all pump, signal, and idler **k**-vectors. That is, from $-0.25$ $m$ to $0.25$ $m$. We then calculate the downconversion amplitudes for each Gaussian beam in the pump distribution in Eq. (5). We then sum these amplitudes, squaring the result to give the total probability density. The procedure for a single Gaussian pump beam is given below, comprising Eqs. (8) to (21). Starting with the grid of $x$ and $y$, angles $\theta_{s(i)}$ and $\varphi_{s(i)}$ were calculated for the signal and idler photons as follows:

$$\theta_s = \tan^{-1}\left(\frac{\sqrt{x^2+y^2}}{z}\right), \theta_i = -\theta_s, \tag{8}$$

$$\varphi_s = \tan^{-1}\left(\frac{x}{y}\right), \varphi_i = \varphi_s + \pi, \tag{9}$$

where $\theta_{s,i}$ and $\varphi_{s,i}$ are the angles shown in Fig. 1, and are defined relative to the optic axis.

The components of the propagation directions $\mathbf{s}_{p/s/i}$ for the pump, signal, and idler, were calculated from $\theta$ and $\varphi$ as follows:

$$s_{\alpha,x} = \sin(\theta_\alpha)\cos(\varphi_\alpha),\ \ s_{\alpha,y} = \sin(\theta_\alpha)\sin(\varphi_\alpha),\ \ s_{\alpha,z} = \cos(\theta_\alpha), \tag{10}$$

where $\alpha = p, s, i$. Additionally, the crystal principal indices of refraction $n_x$, $n_y$, and $n_z$ were calculated for the pump, signal, and idler photons. The Sellmeier equations for BBO were obtained from [1]. The extraordinary and ordinary indices of refraction are then:

$$N_{\alpha,e} = \left(\frac{2}{B + (B^2 - 4C)^{1/2}}\right)^{1/2} \tag{11}$$

$$N_{\alpha,o} = \left(\frac{2}{B - (B^2 - 4C)^{1/2}}\right)^{1/2}, \tag{12}$$

where $\alpha = p, s, i$ and

$$B = \frac{s_{\alpha,x}^2}{n_{\alpha,y}^2 + n_{\alpha,z}^2} + \frac{s_{\alpha,y}^2}{n_{\alpha,x}^2 + n_{\alpha,y}^2} + \frac{s_{\alpha,z}^2}{n_{\alpha,x}^2 + n_{\alpha,y}^2}, \tag{13}$$

$$C = \frac{s_{\alpha,x}^2}{n_{\alpha,y}^2 n_{\alpha,z}^2} + \frac{s_{\alpha,y}^2}{n_{\alpha,x}^2 n_{\alpha,z}^2} + \frac{s_{\alpha,z}^2}{n_{\alpha,x}^2 n_{\alpha,y}^2}. \tag{14}$$

The extraordinary or ordinary indices were assigned to the signal and idler photons depending on which type of phasematching, Type-I or Type-II, was chosen. We can then determine the **k**-vector components for the pump, signal, and idler as follows:

$$k_{\alpha,j} = 2\pi \frac{N_\alpha s_{\alpha,j}}{\lambda_\alpha}, \tag{15}$$

in which $\alpha = p, s, i$ and $j = x, y, z$. The direction vector components $[s_x, s_y, s_z]$ are defined with respect to the optic axis, so these **k**-vectors are given in the crystal frame. The **k**-vector mismatches in the crystal frame of reference are then given by Eq. (16):

$$\Delta k_j = k_{s,j} + k_{i,j} - k_{p,j}, \tag{16}$$

where j = x,y,z. So far, we have worked in the crystal frame because it is convenient to have a consistent frame of reference for plotting. However, due to the non-paraxial nature of the Bessel-Gauss pump beam, we have

chosen to calculate the phasematching amplitudes in the local pump frame ($\mathbf{x}'$, $\mathbf{y}'$, $\mathbf{z}'$) for each paraxial Gaussian beam in the pump distribution (see Fig. 1). To do so, we first convert the $\mathbf{k}$-vector mismatches from the crystal frame ($\mathbf{x}$, $\mathbf{y}$, $\mathbf{z}$) to the pump frame ($\mathbf{x}'$, $\mathbf{y}'$, $\mathbf{z}'$). The transformations between these coordinate systems are given by:

$$\begin{bmatrix} x \\ y \\ z \end{bmatrix} = \begin{bmatrix} \cos(\theta_p)\cos(\varphi_p) & cos(\theta_p)\sin(\varphi_p) & -\sin(\varphi_p) \\ -\sin(\varphi_p) & \cos(\varphi_p) & 0 \\ \sin(\theta_p)\cos(\varphi_p) & \sin(\theta_p)\sin(\varphi_p) & \cos(\theta_p) \end{bmatrix} \begin{bmatrix} x' \\ y' \\ z' \end{bmatrix}. \quad (17)$$

The transformation from the $\mathbf{k}$-vector mismatches in the crystal frame to the $\mathbf{k}$-vector mismatches in the pump frame is then given by:

$$\Delta k_{x'} = \Delta k_x \cos(\theta_p)\cos(\varphi_p) + \Delta k_y \cos(\theta_p)\sin(\varphi_p) - \Delta k_z \sin(\varphi_p), \quad (18)$$

$$\Delta k_{y'} = -\Delta k_x \sin(\varphi_p) + \Delta k_y \cos(\varphi_p), \quad (19)$$

$$\Delta k_{z'} = \Delta k_x \sin(\theta_p)\cos(\varphi_p) + \Delta k_y \sin(\theta_p)\sin(\varphi_p) + \Delta k_z \cos(\theta_p). \quad (20)$$

These $\mathbf{k}$-vector mismatches are substituted into Eq. 21:

$$\Phi_G(\mathbf{k}_p^0, \mathbf{k}_s, \mathbf{k}_i) = \exp\left(\frac{-w_p^2(\Delta k_{x'}^2 + \Delta k_{y'}^2)}{4}\right) \mathrm{sinc}\left(\frac{L_{optic}\Delta k_{z'}}{2}\right) \exp\left(\frac{iL_{optic}\Delta k_{z'}}{2}\right), \quad (21)$$

in which $\Delta k_{x'}$, $\Delta k_{y'}$, and $\Delta k_{z'}$ are the $\mathbf{k}$-vector mismatches in the *x'*, *y'*, and *z'* directions. Here, $L_{\mathrm{optic}}$ is the length of the optical path through the crystal. That is, $L_{\mathrm{optic}} = L_{\mathrm{crystal}}/\cos(\theta_p)$, where $L_{\mathrm{crystal}}$ is the crystal length as measured along its normal. Eq. (21) gives the complex amplitude $\Phi_G(\mathbf{k}_p^0, \mathbf{k}_s, \mathbf{k}_i)$ to generate a signal and idler photon at $\mathbf{k}_s$ and $\mathbf{k}_i$, respectively, from a Gaussian pump beam centered on $\mathbf{k}_p^0$. The first exponential in Eq. (21) corresponds to phasematching transverse to the central pump $\mathbf{k}$-vector. Similarly, the sinc term corresponds to phasematching in the longitudinal direction. The last exponential determines the phase. At this step, we have a 2d grid of $\mathbf{k}_x$ and $\mathbf{k}_y$, with an amplitude $\Phi_G(\mathbf{k}_p^0, \mathbf{k}_s, \mathbf{k}_i)$ for each point on the grid. The corresponding probability is given by $|\Phi_G(\mathbf{k}_p^0, \mathbf{k}_s, \mathbf{k}_i)|^2$.

The plots shown in Fig. 2 and Fig. 7 were produced from the above calculations, with the distinctions between these plots given as follows:

Figures 2(A) and 7(A) give the marginal probability densities for the signal for Type-II and Type-I downconversion, respectively. The amplitude

to produce a signal at $\mathbf{k}_s$ was first calculated for a single central Gaussian pump $\mathbf{k}$-vector $\mathbf{k}_p^0$. For each value of $\mathbf{k}_s$, $\Phi_G$ was determined for all idler $\mathbf{k}$-vectors in the grid. This calculation was then performed for all central $\mathbf{k}$-vectors in the pump distribution, and the outputs were then summed to give the amplitude to produce a photon at our value of $\mathbf{k}_s$ given a Bessel-Gauss pump. We have now determined the amplitude $\Phi_{BG}(\mathbf{k}_s, \mathbf{k}_i)$, given by:

$$\Phi_{BG}(\mathbf{k}_s, \mathbf{k}_i) \propto \sum_{\varphi_p} \Phi_G(\mathbf{k}_p^0(\varphi_p), \mathbf{k}_s, \mathbf{k}_i), \tag{22}$$

where we have approximated the integral over $\mathbf{k}_p^0$ in Eq. (5) with a sum over 750 values of $\mathbf{k}_p^0$ with $\varphi_p$ ranging from 0 to $2\pi$. The marginal probability density for the signal photon is then obtained by taking the absolute square of this amplitude:

$$P(\mathbf{k}_s) = \frac{1}{N} \sum_{\mathbf{k}_{i,x}, \mathbf{k}_{i,y}} \Phi_{BG}(\mathbf{k}_s, \mathbf{k}_i)|^2 \Delta\mathbf{k}_{i,x} \Delta\mathbf{k}_{i,y}, \tag{23}$$

in which N is a normalization factor such that $\sum_{\mathbf{k}_s} P(\mathbf{k}_s)\Delta\mathbf{k}_s = 1$. An identical procedure was used to determine the marginal probability densities $P(\mathbf{k}_i)$ for the idler photon, shown in Figs. 2(B) and 7(B).

# Part II
# Direct Measurement of the Polarization Wavefunction using Optimal Quantum Clones

## 1 Introduction

Fully determining the state of a quantum system is important to predicting the future behaviour of that system. Directly determining the state of a quantum system would require subsequent, noncommuting measurements. By directly, we mean that these measurement results are directly related to the wavefuntion, so the wavefunction can be determined from these measurements without complex calculation. However, performing the first of these measurements collapses the wavefunction and erases information about subsequent, noncommuting measurements, so the second measurement does not provide additional information about the state of the system. Instead, an indirect method is commonly used to determine the state of a quantum system, that is, quantum state tomography [1]. This method is considered indirect because the state of the system is calculated as a "best fit" for the measurement result.

Aharanov, Albert, and Vaidman proposed a method of weakening the measurement interaction until these decoherence effects (i.e. the collapse of the wavefunction following a measurement) are negligible [2]. This allows for two noncommuting measurements to be taken by first measuring weakly in one basis, then making a subsequent strong measurement in an orthogonal basis. Though each trial does not provide sufficient information about the quantum state, a weak value is obtained from an average of multiple trials that post-select on a particular outcome of the second measurement. A joint probability for the two measurement outcomes obtained from this weak measurement technique can be defined by taking a statistical interpretation of these weak values. Provided that the two measurements are performed in orthogonal basis states, this joint probability can completely characterize the density matrix of an arbitrary state. It has been demonstrated experimentally that weak measurement techniques can be used to directly measure quantum states [3].

In 2012, Holger Hofmann proposed that weak values also appear in correlations between cloned quantum systems [4]. That is, the joint probabilities

obtained from weak measurements performed on a single quantum system can also be obtained from the same two measurements performed on optimal quantum clones of this system.

A direct measurement technique to fully characterize the polarization states of light has been demonstrated using weak measurement techniques [5]. In this chapter, we demonstrate that the polarization states of single photons can also be directly determined through strong measurements performed on optimal quantum clones. It is important to note that this technique is significantly different from the weak measurement approach, yet yields the same results.

## 1.1 Summary

The aim of this experiment is to reconstruct the single-photon density matrix that describes the polarization of the target photon. These results will be verified for two input polarization states, those being $|H\rangle$ and $|R\rangle$.

To perform the joint measurement, a photon with a known polarization was cloned on a non-polarizing beam splitter. This cloning method produces photons that are optimal (have the highest permitted fidelity with the target state), symmetric (have the same fidelity), and universal (have the same fidelity regardless of the state of the target photon).

The joint measurements were made in the H/V and D/A bases, with one clone being measured in the H/V basis and the second measured in the D/A basis. These measurements were performed for the symmetric case (successful cloning), anti-symmetric case (no-cloning), and for the case in which these two outcomes were partially mixed in an interferometer. The Dirac distribution obtained from these measurement results was then used to determine the density matrix of the target photon. These results were compared to the expected density matrix of the target state to assess the fidelity of the reconstructed density matrix with that predicted by theory.

# 2 Theory

## 2.1 Measurement and Uncertainty

If we take a quantum state $|\Psi\rangle$ and measure some observable $\hat{A}$, the result is an eigenstate of $\hat{A}$. If this measurement is followed by a measurement of a second, non-commuting observable $\hat{B}$, the result of measurement $\hat{B}$ will be random. The statistics of measurement $\hat{B}$ are changed by the projection of state $|\Psi\rangle$ onto an eigenstate of $\hat{A}$. Moreover, the outcome of making first a measurement of $\hat{A}$ followed by a measurement of $\hat{B}$ will not be the same as the result of a measurement of $\hat{B}$ followed by a measurement of $\hat{A}$. Thus, we cannot gain full information about the state of $|\Psi\rangle$ by making two consecutive, non-commuting measurements.

The precision to which we can know the outcome of these two measurements simultaneously is limited by the Heisenburg Uncertainty Principle. This is one way to understand the change in statistics of $\hat{B}$ following a measurement of $\hat{A}$; if the measurement result of $\hat{A}$ is known perfectly, then the measurement result of $\hat{B}$ cannot be known with any certainty and the result is random. Thus, using traditional measurement techniques, one can't directly determine the state of a quantum system.

A technique known as weak measurement was proposed by Aharanov, Albert, and Vaidman [2]. Weak measurements weaken the measurement interaction until the decoherence effects are negigible. It has been proven experimentally that weak measurement techniques can be used to directly measure quantum states [3]. This is done by performing the first measurement weakly, then performing a second strong (or weak) measurement, post-selecting on a particular outcome for this second measurement. Each trial gives little information about the state of the system, so multiple trials are required to obtain an average result, called the weak value. The weak value the average result of a weak measurement in the sub-ensemble for which a subsequent strong measurement gave a particular result. For example, for some arbitrary state $|\Psi\rangle$, the average result of a weak measurement of $\hat{A}$ with final measurement outcome $|b\rangle$ is given by:

$$\frac{\langle b|\,\hat{A}\,|\Psi\rangle}{\langle b|\Psi\rangle} = \sum_a A_a \frac{\langle b|a\rangle\,\langle a|\Psi\rangle}{\langle b|\Psi\rangle}. \tag{24}$$

From this weak value, a joint probability can be defined for the two-measurement outcome. If these measurements are performed in complementary bases, the complex joint probability completely characterizes the density matrix that describes the state of the quantum system.

Holger Hofmann showed that these joint probabilities also appear in the correlations between cloned quantum systems [4]. The joint probabilities obtained through weak measurements can be determined when the same two measurements are performed on optimal quantum clones of a single system. This gives a method to directly determine the state of a quantum system that is significantly different from weak measurement techniques.

## 2.2 Quantum Cloning

### 2.2.1 Ideal Cloning and the No-Cloning Theorem

Ideally, we would like to be able to produce two perfect copies of a quantum state. This would provide a method to fully measure the polarization state of the original photon, since complementary measurements could be made on each clone (i.e. in the $s_x$ and $s_z$ bases). However, perfect, or ideal, cloning is impossible and is forbidden by the no-cloning theorem [6]. This theorem is of vital importance to quantum communication applications due to its implications for quantum information theory. If a state cannot be copied without additional noise, this provides a means of determining whether an eavesdropper has attempted to copy a transmission. Furthermore, the no-cloning theory avoids violation of information-theoretical principles and prohibits forbidden effects such as superluminal communication. The no-cloning theorem states that no unitary operator exists that can make a perfect copy of any arbitrary target state. As an example, one can imagine a unitary operator U that takes a target state, $|\Psi\rangle$, and a blank state, $|0\rangle$, and copies the state of $|\Psi\rangle$ onto $|0\rangle$, as below:

$$U\,|\Psi\rangle\,|0\rangle = |\Psi\rangle\,|\Psi\rangle\,. \tag{25}$$

States $|H\rangle$ and $|V\rangle$ can then be copied as follows:

$$U\,|H\rangle\,|0\rangle = |H\rangle\,|H\rangle \tag{26}$$

$$U\,|V\rangle\,|0\rangle = |V\rangle\,|V\rangle\,. \tag{27}$$

Quantum operators must be linear, so if U were to act on a state with polarization $1/\sqrt{2}(|H\rangle + |V\rangle)$, then the result should be the same as for a linear combination of $U\,|H\rangle\,|0\rangle$ and $U\,|V\rangle\,|0\rangle$, or:

$$\frac{1}{\sqrt{2}}\left(U\,|H\rangle\,|0\rangle + U\,|V\rangle\,|0\rangle\right) = \frac{1}{\sqrt{2}}\left(|H\rangle\,|H\rangle + |V\rangle\,|V\rangle\right). \tag{28}$$

However, $U(1\sqrt{2}(|H\rangle + |V\rangle)\,|0\rangle$, produces the following:

$$U\left(\frac{1}{\sqrt{2}}\left(|H\rangle + |V\rangle\right)\right)|0\rangle = \frac{1}{2}\left(|H\rangle + |V\rangle\right)\left(|H\rangle + |V\rangle\right) \tag{29}$$

$$= \frac{1}{2}\left(|H\rangle\,|H\rangle + |H\rangle\,|V\rangle + |V\rangle\,|H\rangle + |V\rangle\,|V\rangle\right). \tag{30}$$

These two equations do not give the same result, so this operator cannot be linear (or can only work for orthogonal states, but not for any arbitrary state).

Though perfect, universal cloning is forbidden, the question of how to produce imperfect clones that are as close as possible to the original state (that is, optimal clones) is a fundamental issue in quantum communication. Optimal cloning has potential applications in quantum cryptography [7] and has been shown to improve the performance of measurements on observables over measurements on single systems [8]. Furthermore, in the theory proposed by Hofmann, the weak measurement result arises from measurements performed on optimal quantum clones, even though these are not perfect copies of the original state. One method to produce optimal quantum clones relies on an effect known as Hong-Ou-Mandel interference, which is discussed in the following section.

### 2.2.2 Hong-Ou-Mandel Interference

The no-cloning theorem prevents ideal, or perfect, clones of any arbitrary input state. However, it is possible to make two imperfect copies of any arbitrary input state, in what is known as optimal cloning.

Optimal quantum cloning makes use of an effect known as Hong-Ou-Mandel interference. This effect occurs when two photons are incident on opposite ports of a beam splitter. When one photon is incident on a beam splitter, it has a 50/50 chance of exiting either output port. For two photons incident on a beam splitter, there are four possible outcomes, shown below in Fig. 9.

Labelling the input ports of the beam splitter as $a$ and $b$, and the output ports as $c$ and $d$, the two photons at input ports $a$ and $b$ can be described by the Fock states:

$$a^\dagger b^\dagger\,|00\rangle_{ab} = |11\rangle_{ab}\,, \tag{31}$$

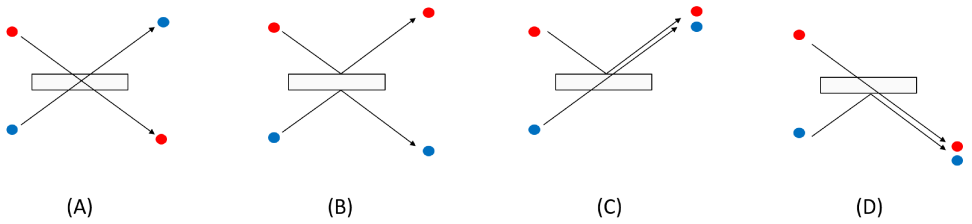


*Figure 9: Four possible outcomes for two photons incident on a non-polarizing beam splitter: (A) both photons are transmitted through the beam splitter; (B) both photons are reflected at the beam splitter; (C) and (D) one photon is transmitted and the other reflected.*

where $|1\rangle$ is the single photon state. Considering the number of photons at the outputs $c$ and $d$, the creation operators $a^\dagger$ and $b^\dagger$ can be rewritten in terms of $c^\dagger$ and $d^\dagger$ as follows:

$$a^\dagger = \frac{1}{\sqrt{2}}\left(c^\dagger + d^\dagger\right), \tag{32}$$

and

$$b^\dagger = \frac{1}{\sqrt{2}}\left(c^\dagger - d^\dagger\right). \tag{33}$$

The output of the beam splitter can then be given by:

$$a^\dagger b^\dagger |00\rangle_{ab} = \frac{1}{2}\left(c^\dagger + d^\dagger\right)\left(c^\dagger - d^\dagger\right)|00\rangle_{cd} \tag{34}$$

$$= \frac{1}{2}\left(c^\dagger c^\dagger + c^\dagger d^\dagger - d^\dagger c^\dagger - d^\dagger d^\dagger\right)|00\rangle_{cd}. \tag{35}$$

If the two photons entering the beam splitter are identical, then the terms $c^\dagger d^\dagger$ and $d^\dagger c^\dagger$ will cancel out. That is, there is no distinction between the case in which the photon at $a$ exits at $c$ and the photon at $b$ exits at $d$, and the case in which the photon at $a$ exits at $d$ and the photon at $b$ exits at $c$ (cases (A) and (B) in Fig.9). There are then only two possible outputs; two photons exit at output $c$, or two photons exit at output $d$:

$$\frac{1}{2}\left(c^{\dagger 2} - d^{\dagger 2}\right)|0_c 0_d\rangle = \frac{1}{2}\left(|2_c 0_d\rangle - |0_c 2_d\rangle\right). \tag{36}$$

In this case, the two photons "bunch", i.e. they always exit at the same port of the beam splitter. This phenomenon is known as Hong-Ou-

Mandel interference. Conversely, if the two photons are not identical, the four outputs shown in Fig. 9 may occur with equal probability.

Hong-Ou-Mandel interference produces what is known as a Hong-Ou-Mandel dip at the output of the two beam splitter ports. If two identical photons are directed into opposite beam splitter ports with a delay line in one arm, detectors placed at the output ports will see a dip in coincidences when the two photons arrive at the beam splitter at the same time. When the lengths of the two arms are unequal, the photons arrive at different times and are therefore distinguishable, and will then exit in one of the four ways shown in Fig. 9. When the lengths of the two paths into the beam splitter are the same, the photons are indistinguishable and will always bunch, so there are no coincidences at the two output detectors.

### 2.2.3 Optimal, Symmetric, Universal Cloning

One method of producing optimal quantum clones relies on Hong-Ou-Mandel interference [9]. For this method, two photons are sent into opposite ports of a non-polarizing beam splitter. One photon in an arbitrary, known polarization state, $|\Psi\rangle$, is sent into one input port of the beam splitter. A maximally mixed state, the 'blank' state, is sent into the other port of the beam splitter. A maximally mixed state is a classical statistical mixture in which all quantum states have equal probability; the density matrix describing this state is proportional to the identity matrix. When these two photons exit the same port of the beam splitter, the cloning operation is considered a success.

This cloning process mixes two cases: one in which two identical photons exit the same port (with probability 2/3), and the case in which two orthogonally polarized photons exit the same port (with probability 1/3). These probabilities arise because the mixed photon is identical to the target photon 50% of the time, and orthogonal to the target photon 50% of the time. If we consider the output at only one beam splitter port, when the two photons are identical, they will exit together at this port 50% of the time. When the two photons are orthogonal, they will exit this port together 25% of the time. Since we are considering only the case in which two photons exit a particular output port, the probability of these photons being identical is twice the probability of them being orthogonally polarized, which results in the 2/3 and 1/3 probabilities, respectively, for these two cases.

The resulting output is an entangled state in which the state of each photon is given by:

$$\rho_{cd} = \frac{2}{3}(\Pi^{+}_{cd}\rho\otimes I\Pi^{+}_{cd}), \tag{37}$$

in which $\rho = |\Psi\rangle\langle\Psi|$, where $|\Psi\rangle$ is the target state, $\Pi^{+}$ is the symmetric projector, and the state of the maximally mixed state is $\rho = I/2$. The cloning operation can then be thought of as a projection of the two input states (the target state and maximally mixed state) onto the symmetric subspace.

The fidelity of these clones with respect to the original target state is 5/6, or 83%. Fidelity is a measure of the 'closeness' of two quantum states, where 1 would indicate the the two states are identical, and 0 would indicate orthogonal states. This represents the maximum possible fidelity for these clones allowed by quantum mechanics, which was derived in [10].

This method of cloning is optimal, symmetric, and universal. The clones are considered optimal in that they have the maximum possible fidelity allowed by quantum mechanics. This cloning method is considered symmetric because the two clones are in the same state, and therefore have the same fidelity with respect to the target state. This method of cloning is also universal; unlike perfect cloning, which is possible for only orthogonal states, this method of cloning works for any arbitrary input state.

### 2.2.4 Cloning and Symmetry

To fully reconstruct the density matrix of the target state, the two photons are measured after undergoing one of four symmetry operations. These are the symmetric, anti-symmetric, and $\sqrt{\text{SWAP}}$ operations (where the $\sqrt{\text{SWAP}}$ may have a phase of $\pm\pi/2$). These operations are discussed below.

The symmetric and anti-symmetric projectors act on two systems, A and B, and project onto either the symmetric or anti-symmetric subspace. Their properties are as follows:

$$\Pi^{+}_{AB} + \Pi^{-}_{AB} = I_{AB} \tag{38}$$
$$\Pi^{\pm}_{AB}\Pi^{\pm}_{AB} = \Pi^{\pm}_{AB} \tag{39}$$
$$\Pi^{\pm}_{AB}\Pi^{\mp}_{AB} = 0, \tag{40}$$

where $I_{AB}$ is the identity operator on both systems, $\Pi^{+}$ is the symmetric projector, and $\Pi^{-}$ is the anti-symmetric projector.

The beam splitter used for the cloning operation transforms the symmetry projector to a parity projector. That is, a single photon present at

each output port represents odd parity and thus a projection onto the anti-symmetric subspace; two photons present at either output port represents even parity and thus a projection onto the symmetric subspace.

When the two input states, the target state and mixed state, exit the same port of the beam splitter, the cloning is considered a success, and the two photons are in the entangled state $\rho_{CD}$ given in Eq. (37). These photons can be split on a second non-polarizing beam splitter for tomographic measurement.

The SWAP operator, $S_{AB}$, swaps the state of the two systems, i.e. $\rho_A \otimes \rho_B \rightarrow \rho_B \otimes \rho_A$. Partial mixing of the two states can be achieved with a partial SWAP operation, $U_{AB}(\phi)$:

$$U_{AB}(\phi) = \Pi^+_{AB} + e^{i\phi}\Pi^-_{AB}. \tag{41}$$

When $\phi = \pi/2$, this gives a $\sqrt{\text{SWAP}}$ operation, which mixes the symmetric and anti-symmetric cases. The $\sqrt{\text{SWAP}}$ operator can be expressed as:

$$\Pi^i_{AB} = \frac{1}{2}\left[I_{AB} + iS_{AB}\right]. \tag{42}$$

This $\sqrt{\text{SWAP}}$ operation can be performed with an interferometer posessing a $\pi/2$ phase between the two interfering paths. One such setup was proposed by Fiurasek et. al, which uses a Mach-Zehnder interferometer to perform the $\sqrt{\text{SWAP}}$ operation [11]. We use this setup in a displaced Sagnac configuration for the $\sqrt{\text{SWAP}}$.

### 2.2.5 Cloning and Weak Measurement

In 2012, Hofmann demonstrated theoretically that the joint probabilities obtained from weak measurement techniques also appear in correlations between optimal quantum clones [4].

Recall that the optimal quantum clones exit the beam splitter in entangled state $\rho_{CD}$:

$$\rho_{CD} = \frac{2}{3}[\Pi^+\rho \otimes I\Pi^+],$$

where $\Pi^+$ is the symmetry projector, $\rho$ is the density matrix of the target state, and I is the identity matrix.

For two incompatible measurements performed on the optimal quantum clones, e.g. $\pi_x = |x\rangle\langle x|$, and $\pi_y = |y\rangle\langle y|$,the result of these two measurements is as follows:

$$\langle \pi_x \otimes \pi_y \rangle_{\rho_{CD}} = \mathrm{Tr}\left[\pi_x \otimes \pi_y \rho_{CD}\right] \tag{43}$$

$$= \frac{1}{2(d+1)} \left[ \mathrm{Prob}(x) + \mathrm{Prob}(y) + 2Re\left[ \langle \pi_x \pi_y \rangle_\rho \right] \right], \tag{44}$$

where d is the dimension of the Hilbert space, Prob(x) is the probability of measurement result x, Prob(y) is the probability of measurement result y, and the weak average is:

$$\langle \pi_x \pi_y \rangle_\rho = Tr\left[\pi_x \pi_y \rho\right]. \tag{45}$$

This weak average is the result of measuring $\pi_x \pi_y$ on the single photon with state $\rho$, making first a weak measurement of $\pi_x$ followed by a strong (or weak) measurement of $\pi_y$ [12].

The real part of the weak average, then, emerges in joint measurements performed on optimal quantum clones. To obtain the imaginary part of the weak average, the $\sqrt{\mathrm{SWAP}}$ operation is used to interfere the symmetric and anti-symmetric cases (i.e. cloning and non-cloning cases). In this case, the state of the two photons is given by $\rho_{CD}^{(i)}$, which has a similar form to that of $\rho_{CD}$:

$$\rho_{CD}^{(i)} = \Pi_{CD}^{i} \rho \otimes I \Pi_{CD}^{i}, \tag{46}$$

where $\Pi_{CD}^{i}$ is the $\sqrt{\mathrm{SWAP}}$ operator defined in Eq. (42). In this case the weak average that emerges from the same joint measurement is:

$$\langle \pi_x \otimes \pi_y \rangle_{\rho_{CD}^{(i)}} = \frac{1}{2(d+1)} \left[ Prob(x) + Prob(y) + 2Re[i \langle \pi_x \pi_y \rangle_\rho] \right]. \tag{47}$$

The Dirac distribution for the target photon can then be determined when these two measurements, $\pi_x$ and $\pi_y$, are made for four symmetry operations:

$$\langle \pi_x \pi_y \rangle_\rho = \frac{d+1}{2} [P^{+1}(x,y) - P^{-1}(x,y) - i[P^{+i}(x,y) - P^{-i}(x,y)]]. \tag{48}$$

Here, $P^{+1}(x,y)$ is the probability of jointly obtaining measurement results x and y when the two photons are projected onto the symmetric subspace; $P^{-1}(x,y)$ is the probability of jointly obtaining measurement results

x and y when the two photons are projected onto the anti-symmetric subspace; $P^{+i}(x,y)$ is the probability of jointly obtaining measurement results x and y when the two photons undergo a $\sqrt{\text{SWAP}}$ operation; and $P^{-i}(x,y)$ is the probability of jointly obtaining measurement results x and y when the two photons undergo a $\sqrt{\text{SWAP}}$ operation with a phase of $-\pi/2$ between them. The real part of the Dirac distribution is obtained from the term $P^{+1}(x,y) - P^{-1}(x,y)$, and the imaginary part of the Dirac distribution is obtained from the term $P^{+i}(x,y) - P^{-i}(x,y)$. By making these four measurements on optimal quantum clones, the polarization state of the target photon can be fully reproduced.

It is important to note that this approach is very different from the weak measurement technique, and yet the same result still appears in the correlations between the two optimally cloned photons. Also important to note is that the result appears despite the fact that the clones are not perfect copies of the input state.

## 2.3 Summary

In this section, we have introduced the concept of optimal quantum cloning and its potential application for the direct measurement of quantum states. These optimal quantum clones are produced on a non-polarizing beam splitter by sending a photon with a target polarization into one beam splitter port and a maximally mixed state into the other beam splitter port.

In the following section, we simulate the propagation of photon pairs through a non-polarizing beam splitter, to simulate the cloning operation, and propagation through an interferometer with a $\pi/2$ phase between the two arms, to simulate a $\sqrt{\text{SWAP}}$ operation. We verify, through these simulations that the joint probability in Eq. (44) appears in joint measurements performed on optimal quantum clones, and that the joint probability in Eq. (47) appears for joint measurements performed on the two optimal clones after they have been interfered with a phase of $\pi/2$ between the two interfering arms. These results are used to verify that the experimental setup described in Section 4 will allow us to reconstruct the polarization state of the target photon.

# 3 Theoretical Modelling and Simulation

It has been demonstrated theoretically that weak values appear in correlations between cloned quantum systems [4]. In this section, we demonstrate that these results can be obtained experimentally by simulating the propagation of photon pairs through the experimental setup described in Section 4. These simulations were performed using a Maple code written by Terry Rudolph. This code models multiphoton optical states through beam splitters, phase-shifters, and polarization rotators.

In Section 3.1, we calculate the real and imaginary parts of the Dirac distribution for a single photon. We then calculate the probability of jointly obtaining two measurement results, H and T, on two copies of this state.

In Section 3.2, we simulate the process of optimal quantum cloning by simulating the propagation of two photons (one with a target polarization state, and the other in a maximally mixed state) through a non-polarizing beam splitter. We confirm that the probability of jointly measuring H and T on these optimal clones agrees with that predicted in Section 3.1. We then simulate the propagation of these photon pairs through an interferometer with a phase of $\pi/2$, to perform a $\sqrt{\text{SWAP}}$, and confirm that the imaginary part of the probability of jointly measuring H and T agrees with the probability derived in Section 3.1.

## 3.1 Dirac Distribution of a Qubit

In this section we calculate the Dirac distribution of a single photon with an arbitrary polarization. The Dirac distribution is a complex, discrete quasi-probability distribution that gives the same information as the density matrix. Though the Dirac distribution is not commonly used to describe quantum states, it is convenient for this measurement technique because the components of the Dirac distribution may be determined directly from our measurements. For some photon with a polarization state given by density matrix $\rho$, the components of the Dirac distribution are given by:

$$\begin{aligned} D(a,b) &= Tr\left[\pi_a \pi_b \rho\right] \\ &= Tr\left[\left|a\right\rangle \left\langle a\right| \left|b\right\rangle \left\langle b\right| \rho\right] \\ &= Tr\left[\left\langle b\right| \rho \left|a\right\rangle \left\langle a\right| \left|b\right\rangle\right] \\ &= \left\langle b\right| \rho \left|a\right\rangle \left\langle a\right| \left|b\right\rangle . \end{aligned} \tag{49}$$

Here, $\pi_a$ and $\pi_b$ represent two simultaneous measurements, $\left|a\right\rangle \left\langle a\right|$ and $\left|b\right\rangle \left\langle b\right|$ performed on $\rho$.

In our simulation, we calculated the Dirac distribution for a photon with an arbitrary polarization given by $|\Psi\rangle$:

$$|\Psi\rangle = a\,|H\rangle + b|V\rangle. \tag{50}$$

The density matrix that describes the polarization of this photon is as follows:

$$\rho = \begin{bmatrix} aa^* & ab^* \\ a^*b & bb^* \end{bmatrix}. \tag{51}$$

Two measurements were performed on this state, these measurements being H and T, which are defined as follows:

$$H = \begin{bmatrix} 1 \\ 0 \end{bmatrix} \tag{52}$$

$$T = \begin{bmatrix} \cos\theta \\ \sin\theta \end{bmatrix}, \tag{53}$$

where H is a projection onto polarization state $|H\rangle$ and T is a measurement in a rotated basis, where the rotation is through angle $\theta$. The Dirac distribution is calculated as follows:

$$D(H,T) = H^\dagger \rho T T^\dagger H = \cos\theta(|a|^2\cos\theta + ab^*\sin\theta). \tag{54}$$

The real and imaginary parts of the Dirac distribution are then:

$$Re[D(H,T)] = \frac{1}{2}\cos\theta(2|a|^2\cos\theta + (ab^* + a^*b)\sin\theta) \tag{55}$$

$$Im[D(H,T)] = \frac{i}{2}(a^*b - ab^*)\sin\theta\cos\theta. \tag{56}$$

From the theory proposed by Hofmann, the real part of the Dirac distribution is related to the clone measurements by:

$$P(H,T) = \frac{1}{2(d+1)}[Prob(H) + Prob(T) + 2Re[\rho_c(H,T)], \tag{57}$$

where P(H,T) is the probability of jointly measuring H for one of the cloned photons and T for the second cloned photon, Prob(H) is the probability of measurement result H on the input photon, Prob(T) is the probability of measurement result T on the input photon, and $\rho_c(H,T)$ is the real part

of the Dirac distribution D(H,T) for the input state. The probability of measurement result H is given by:

$$Prob(H) = H^\dagger \rho H = |a|^2. \tag{58}$$

The probability of measurement result T is given by:

$$Prob(T) = T^\dagger \rho T = |b|^2 + (|a|^2 - |b|^2)\cos\theta^2 + (ab^* + a^*b)\sin\theta\cos\theta. \tag{59}$$

The real part of the joint measurement, P(H,T), performed on $|\Psi\rangle$ will then be:

$$P(H,T) = \frac{1}{6}[H^\dagger \rho H + T^\dagger \rho T + 2Re[D(H,T)]] \tag{60}$$

$$= \frac{1}{6} + \frac{1}{2}|a|^2\cos\theta^2 - \frac{1}{6}|b|^2\cos\theta^2 + \frac{1}{3}(ab^* + a^*b)\sin\theta\cos\theta \tag{61}$$

$$= \frac{1}{6}[1 + (3|a|^2 - |b|^2)\cos\theta^2 + 2Re[a^*b]\sin 2\theta]. \tag{62}$$

The imaginary part of the joint measurement, which emerges when a $\sqrt{\text{SWAP}}$ operation is performed on the two photons, is given by:

$$P_{\sqrt{\text{SWAP}}}(H,T) = \frac{1}{6} + \frac{1}{6}(|a|^2 - |b|^2)\cos\theta^2 + \tag{63}$$

$$\frac{1}{6}(ab^* + a^*b)/\sin\theta\cos\theta + \frac{i}{6}(a^*b - ab^*)\cos\theta\sin\theta. \tag{64}$$

These two quantities, P(H,T) and $P_{\sqrt{\text{SWAP}}}(H,T)$ are the theoretical probabilities to jointly obtain measurement results H and T when these measurements are performed on a photon with polarization state given by $|\Psi\rangle$.

## 3.2 Simulation of Optimal Cloning and $\sqrt{\text{SWAP}}$ Operation

To test whether the proposed setup will give these results, the experimental setup was simulated in Maple. This code allows for specification of the number and polarization of photons in each mode and allows for propagation through non-polarizing beam splitters and waveplates, so the propagation of the two photons can be simulated through the full interferometer.

For simplicity, the displaced Sagnac interferometer is shown below as a Mach-Zehnder (as in Fig. 16-(B)). This allows the four beam splitters to

be labeled with more clarity. The four beam splitters are labeled BS1, BS2, BS3, and BS4, where BS1 is the first beam splitter in the interferometer. The detectors for measurements 1, 2, and 3 are labeled D1, D2, and D3, respectively.

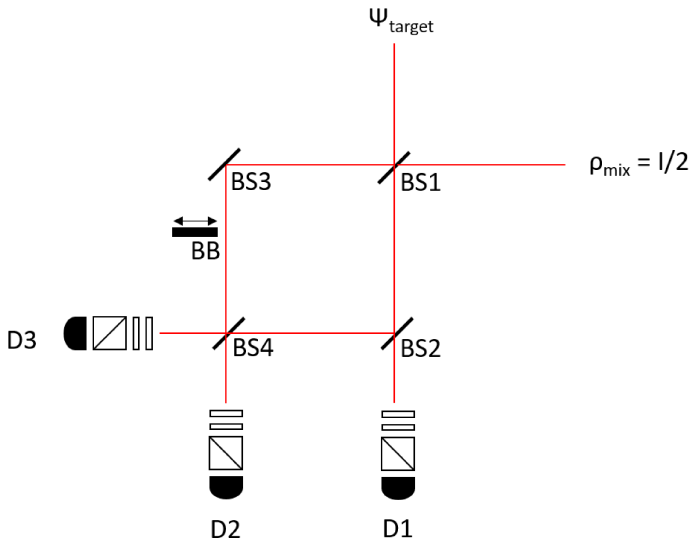


*Figure 10: Setup for theoretical modeling. The interferometer is modeled as a Mach-Zehnder for simplicity. For a measurement of the real part of the Dirac Distribution D(H,T), the photons are sent into the first beam splitter, and the output of one port passes through a second NPB. A measurement of H is made at detector D1 and a measurement of T is made at detector D2. For the imaginary part of Dirac Distribution D(H,T), the two photons are passed through the full interferometer, with the same measurements made at detectors D1 and D2.*

To simulate the real part of the joint measurement, we start with one photon with target state $|\Psi\rangle_{target} = a\,|H\rangle + b\,|V\rangle$, and the second photon in a mixed state. The mixed state was input by running the code twice, once with input state $|H\rangle$ and again with input state $|V\rangle$. These two photons are sent into opposite ports of beam splitter BS1, then the output from one port of the beam splitter is sent to a BS2 (where bunching photons are split for measurement). This is akin to inserting the beam block (labeled BB) and making measurements at D1 and D2 in the setup shown in Figure 10. We then measure H at detector D1 and T at detector D2. To determine the joint measurement result, we take the probability of getting a measurement of H at each output simultaneously (where the output at D2 is rotated through

angle $\theta$ prior to a measurement of H to give the rotated measurement T). The resulting probability is:

$$P_{sim}(H,T) = \frac{1}{32}|a|^2\cos\theta^2 + \frac{1}{32}|a|^2 + \frac{1}{32}|2a^*\cos\theta - b^*\sin\theta|^2 \tag{65}$$

$$= \frac{1}{32}[1 + (3|a|^2 + |b|^2)\cos\theta^2 + 2Re[a^*b]\sin 2\theta] \tag{66}$$

$$= \frac{3}{16}P(H,T). \tag{67}$$

The simulated probability of jointly obtaining measurement results H and T is equal to the theoretical probability derived from the Dirac distribution, up to a numerical factor. This factor arises due to losses in the interferometer (i.e. post-selection on only one output port of the cloning beam splitter, BS1).

To determine the imaginary part of the Dirac Distribution, the beam block, BB, was removed to allow photons to pass through both interferometer arms. As above, the two photons are sent through the cloning beam splitter (BS1). The two output modes of BS1 were each sent through a second beam splitter (those being BS2 and BS3 in Fig. 10). The outputs of BS2 and BS3 were then recombined at the final beam splitter (BS4), with a phase of $\pi/2$ added to one of the interferometer arms. A measurement of H was taken at one output of BS2, and a rotated measurement, T, was taken at one output BS4. The probability of simultaneously making a measurement of H at BS2, and of H at BS4 (following a polarization rotation through angle $\theta$) is given below:

$$P_{\sqrt{\text{SWAP}}sim}(H,T) = \frac{1}{16}|a|^2 - \frac{1}{16}|a|^2\cos^2\theta + \frac{1}{32}|2ia\cos\theta + b\sin\theta - ib\sin\theta|^2 \tag{68}$$

$$= \frac{1}{6}[1 + (|a|^2 - |b|^2) + Im[ab^*]\sin 2\theta] \tag{69}$$

$$= \frac{3}{16}P_{\sqrt{\text{SWAP}}}(H,T). \tag{70}$$

The simulated probability of getting measurement results H and T after performing a square root swap on the optimal quantum clones is the same as the theoretical probability derived from the Dirac Distribution, up to a constant factor. This factor arises, as for the real part, from losses in the interferometer, specifically at the output of BS3 and at the output of BS4 at which we do not make a measurement.

### 3.3 Summary

In this section, we simulated in Maple the propagation of photon pairs through an interferometer. We confirmed that the real and imaginary parts of the probability P(H,T), that is, the probably of jointly obtaining measurement results H and T on an arbitrary state, can be obtained by performing the same two measurements on optimal quantum clones. The real part of this probability is obtained through measurements performed on two optimal quantum clones after exiting the cloning beam splitter, and the imaginary part of this probability appears in the joint measurement performed on the two photons after they have been interfered with a $\sqrt{\text{SWAP}}$ operation. This confirms that the experimental setup, described in Section 4, will allow us to measure the Dirac distribution of the target state. It is then possible to reconstruct the density matrix of the target state from this Dirac distribution.

After confirming the theoretical results of this simulation, we confirmed this result experimentally. Details of the experimental setup are given in Section 4.

# 4 Experimental Setup

A diagram of the full experimental setup is shown below in Fig. 11.

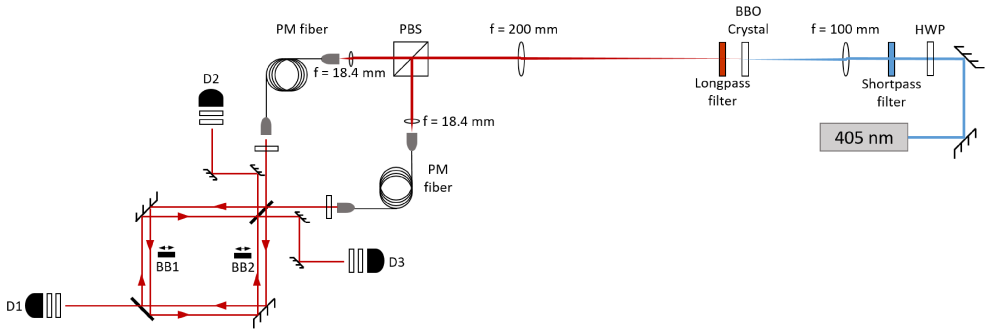


*Figure 11: Experimental setup. Photon pair production is pumped by a 405 nm laser diode. The pump beam is focused into a 1 mm BBO crystal to produce signal and idler photons at 810 nm. The photons are orthogonally polarized and are split at a polarizing beam splitter before being coupled to polarization maintaining fibers. These two photons are then prepared and sent into a non-polarizing beam-splitter to produce the optimal quantum clones, which are then sent through a displaced Sagnac Interferometer and measured at the three detectors shown on the left.*

For simplicity, the setup will be divided into four sections: production of photon pairs at 810 nm; arrival at the cloning beam splitter and measurement of the HOM dip; interference in a displaced Sagnac interferometer; and collection for measurement.

Photon pairs were produced through spontaneous parametric downconversion. These photon pairs were separated on a polarizing beam splitter and coupled into polarizing maintaining fibers to decouple the photon pair production from the cloning device. The photon pairs were then aligned into a non-polarizing beam splitter. Observation of a Hong-Ou-Mandel dip was used to confirm that the photons arrived at this beam splitter at the same time. A displaced Sagnac interferometer was then constructed to interfere the symmetric and anti-symmetric outputs of this beam splitter.

This experimental setup allows us to directly determine the density matrix of a target photon by performing measurements of optimal quantum clones of that photon. Optimal quantum clones are produced at the first non-polarizing beam splitter. The interferometer arms may then be blocked, as required, for the four symmetry operations described in Section 2.2.4. Projective measurements of polarization were performed for each of these four interferometer configurations, corresponding to the four terms in Eq.

(48). The Dirac distribution for the target photon was calculated from these measurement results, and the density matrix describing the target photon state was reconstructed from the Dirac distribution.

In this section, we describe in detail each part of the experimental setup and the tests used to optimize the setup at each stage. A discussion of the efficacy of the cloning device and the joint measurement follow in Section 5.

## 4.1 Photon Pair Production

Photon pairs were produced through spontaneous parametric downconversion (SPDC). This is a nonlinear optical process in which a pump photon spontaneously decays within a second-order nonlinear crystal to produce two photons at lower frequencies. These two photons are commonly referred to as signal and idler. This process conserves energy and momentum, and the two down-converted photons are correlated both spatially and temporarily. These photons are produced in what is known as degenerate, Type-II SPDC, which means that the two down-converted photons have the same frequency but orthogonal polarizations.

The pump laser was a 40 mW CW laser diode at 405 nm, which was chosen for its wavelength stability, with a central wavelength tolerance of $\pm$ 1 nm, and for its narrow bandwidth, which was less than 0.06 nm. For degenerate downconversion, the photon pairs were produced at 810 nm. To ensure that no higher wavelength components were present in the beam the pump was sent through a shortpass filter with a cut-off wavelength of 700 nm. This ensured that no higher wavelength light from the pump exits the downconversion crystal with the single photons at 810 nm.

A half-wave plate was placed after the pump beam to align the pump polarization horizontally with respect to the optical table. This pump beam was focused into a uniaxial, second order nonlinear crystal ($\beta$-Barium Borate, or BBO), cut for Type-II downconversion. The crystal was placed on a rotating mount to allow for tuning of the phasematching angle. A 100 mm plano-convex lens was used to focus the pump into the BBO crystal. This focal length was chosen to give a FWHM of 25 $\mu$m at the crystal face.

A longpass filter, with cut-off wavelength 450 nm, was placed after the BBO crystal to remove the pump photons that did not contribute to phasematching. As Type-II downconversion produces signal and idler photons with orthogonal polarizations, the horizontally polarized pump beam produces one downconverted photon with horizontal polarization, and one with vertical polarization. The photons were separated on a polarizing beam splitter, then each photon was coupled into a polarization maintaining (PM)

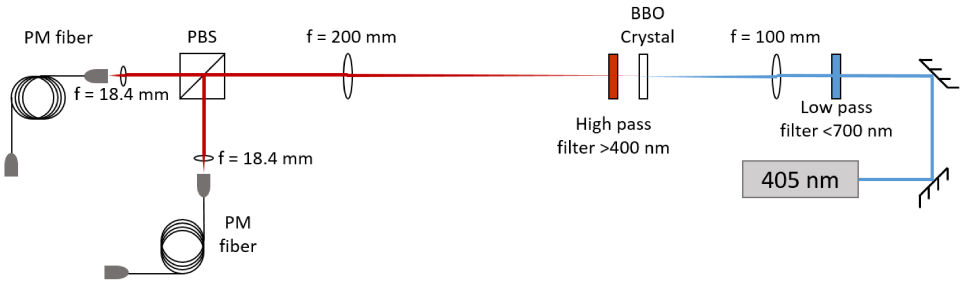


*Figure 12: Photon pair production setup. Photons are produced through spontaneous parametric downconversion (SPDC). The pump laser is a 405 nm laser diode, which is filtered with a shortpass filter that transmits only wavelengths below 700 nm. The pump beam is focused into a BBO crystal to produce photon pairs with orthogonal polarizations. The pump beam is filtered out using a longpass filter placed after the BBO crystal, to remove wavelengths below 450 nm. The photon pairs were then split on a polarizing beam splitter and coupled into two polarization maintaining fibers.*

fiber. These fibers were chosen because they will maintain a linear polarization during propagation. The target photon polarization was then set with a combination of half-wave plates and quarter-wave plates.

Polarization maintaining fibers were chosen to allow a specific polarization to be set as a target state for the cloning operation. When the polarization of photons entering the polarization maintaining fibers are aligned along the fiber axis, these fibers will maintain a linear polarization during propagation. This was achieved using a classical alignment beam, that is, an 810 nm laser diode. This laser diode entered the setup through the remaining port of the PBS at which the photon pairs are split. The polarization of the classical alignment laser was set to 45° so that the beam was equally split at the PBS, and the classical light was then coupled into both of the PM fibers.

The optic axis of the BBO crystal was aligned to maximize the number of coincidences detected at the output of the two PM fibers in Fig.12. The singles counts were maximized to 77 000 counts per second in the reflected arm (fiber F2), and 50 000 counts per second in the transmitted arm (fiber F1), with 16 750 coincidences per second between the two arms.

## 4.2 Hong-Ou-Mandel Interference

Half-wave plates were placed at the output port of each of these polarization-maintaining fibers to set the polarization of each photon as they enter the

cloning beam splitter. The two input beams (labeled 'F1' and 'F2' in Fig. 13) were aligned into a non-polarizing beam splitter (NPB). This alignment was optimized by maximizing the visibility of Hong-Ou-Mandel interference.

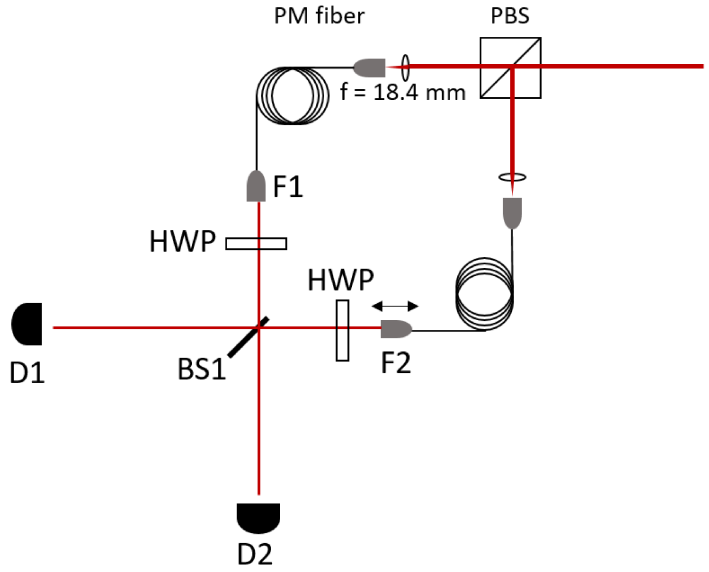


*Figure 13: Setup for Hong-Ou-Mandel interference. Photon pairs are emitted from the polarization maintaining fibers and have their polarizations set by half-wave plates placed at the output of each fiber. The half-wave plates are aligned to give both photons horizontal polariztion. The two photons are aligned into a non-polarizing beam splitter and the output from each beam splitter port is collected by a fiber-coupled avalanche photodiode (APD). The dip is produced by moving the fiber F2 output position to change the time delay between the two photons arriving at the beam splitter. For each translation stage position, the coincidence counts are measured between the two beam splitter outputs.*

The non-polarizing beam splitter was first tested to ensure that the transmission and reflection coefficients were equal and polarization independent. To test that the beam splitter was in fact 50/50, each beam was sent into the beam splitter separately and the transmitted power and reflected power were measured on a photodiode. The percent transmitted (or reflected) was then determined by taking the power of the transmitted (reflected) beam divided by the total power. From this, the reflected intensity as found to be 51% and transmitted intensity to be 49%. To determine the polarization dependence of the non-polarizing beam splitter, the output power was monitored while the half-wave plate was taken through a full rotation.

Following this characterization, both beams were aligned into the beam splitter to maximize the visibility of classical and single-photon interference. Two mirrors were placed after each of the PM fibers to allow control of the position and angle of each beam. Prior to testing the quantum interference, classical interference was tested at the cloning beam splitter using an 810 nm laser diode for alignment. This configuration is shown in Fig. 14. In this configuration, we have formed a Mach-Zehnder interferometer; the output from the classical laser is equally split on the PBS by setting its polarization to 45°, and these two components are then recombined on the cloning beam splitter. Maximizing the classical interference observed at one output of the beam splitter allows us to confirm that the inputs from fibers F1 and F2 are well overlapped on the cloning beam splitter prior to testing the quantum interference by observing the Hong-ou-Mandel dip.

To measure the Hong-Ou-Mandel dip, the output of one fiber was placed on a translation stage. This stage was motorized and computer controlled. By moving the translation stage, a time delay was introduced between the two photons arriving on the beam splitter. This was used to find the point of maximum classical interference, and in scans of the Hong-Ou-Mandel dip using the single photon source. The output of fiber F1 was aligned through the NPB to ensure that the angle of the beam would not change when the translation stage was moved. The second input beam was then aligned on the first, and classical interference was observed on an oscilloscope by placing a photodiode at one output face of the NPB.

The classical interference was maximized for a particular position of the translation stage, then the stage was scanned across its full range to find the position at which there was a peak in the classical visibility. At this position, the interference was again maximized by aligning the second fiber input with respect to the first. The classical interference was peaked to 94%.

To observe the single-photon interference, the two outputs of the NPB were then coupled into single-mode fibers and collected at Avalanche Photodiodes (APDs). A coincidence counter monitored the coincidence counts as the time delay was adjusted between the two photons arriving at the non-polarizing beam splitter. This allowed for a scan of the Hong-Ou-Mandel dip using the single-photon source. With the single photon source, the photons exiting the two NPB ports were collected using fiber-coupled APDs at each output port of the beam splitter. The time delay between the two photons was adjusted by changing the position of the translation stage, and the number of coincidences between the two APDs were measured for each translation stage position.

The Hong-Ou-Mandel dip is shown in Fig. 15. The half-wave plates

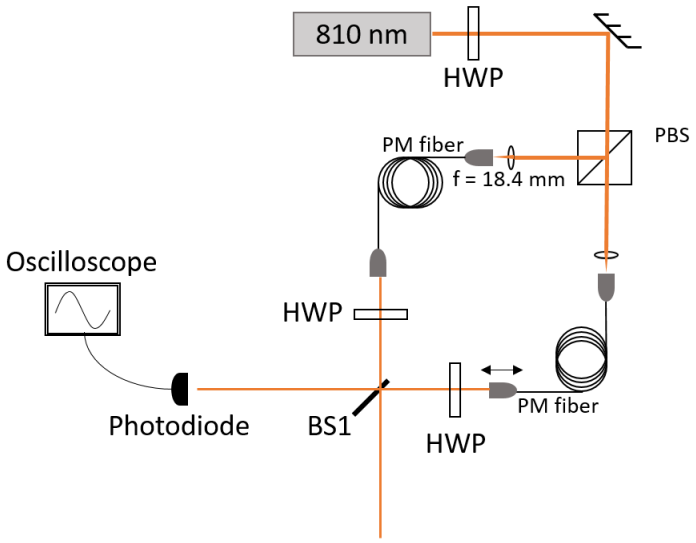


*Figure 14: Setup for classical interference. An 810 nm laser diode is sent into the free polarizing beam splitter (PBS) input port and coupled to the same polarization maintaining fibers as for the single-photon interference. Classical interference is observed with a photodiode placed at one output port of the non-polarizing beam splitter (BS1). Interference was observed on an oscilloscope.*

after fibers F1 and F2 were set to transmit horizontally polarized single photons. The output of each beam splitter port was aligned into a fiber-coupled APD to collect the photons exiting the beam splitter, as shown in Fig. 13. These APDs were connected to a coincidence counter to determine the singles counts at each detector, as well as the coincidence counts within a 10 ns window.

The time delay between the two photons was controlled by moving the translation stage in steps of 3 $\mu$m. At each step, the coincidences were collected for a duration of 1 s.

The visibility of the dip was calculated as follows:

$$Visibility = \frac{max\ coincidences - min\ coincidences}{max\ coincidences + min\ coincidences}. \tag{71}$$

Using Eq. (71), the dip visibility was calculated to be 94%, with a FWHM of 53.5 $\mu$m. Ideally, the Hong-Ou-Mandel dip could have a visibility of 100%. The reduction in visibility may be due to slight differences in collimation at the outputs of fibers F1 and F2, which can affect the spatial overlap at the cloning beam splitter BS1.

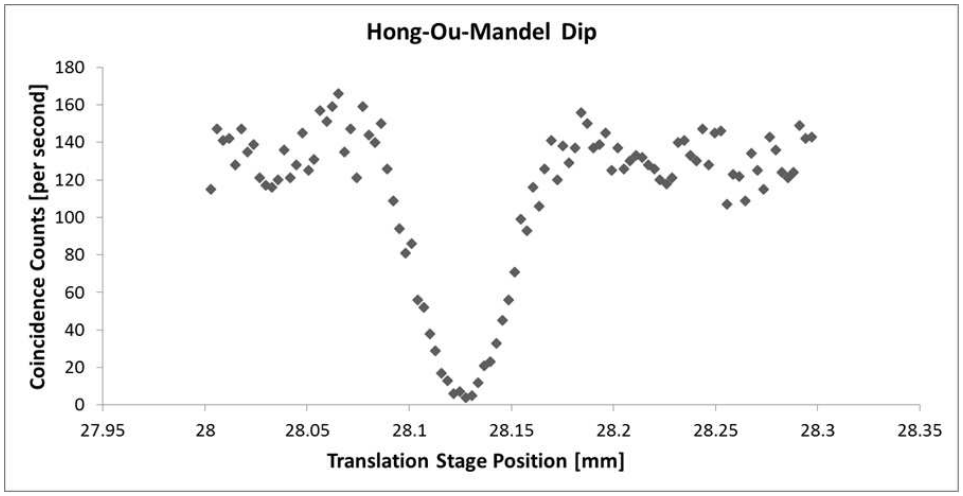


*Figure 15: Hong-Ou-Mandel (HOM) dip. The two single photons are horizontally polarized and are interfered on a non-polarizing beam splitter. The number of coincidence counts in 30 seconds are plotted as a function of the translation stage position (in mm). Two HOM dips are displayed: in black, the HOM dip as measured with only a highpass filter placed after the crystal; and, in red, the HOM dip as measured with an 810 nm bandpass filter with a bandwidth of ± 10 nm.*

### 4.3 Displaced Sagnac Interferometer

To measure the imaginary part of the joint probability, the symmetric and anti-symmetric outputs are interfered using a $\sqrt{\text{SWAP}}$ gate. The symmetric output is one in which the photons exit together at one port of the beam splitter (a successful cloning operation), and the anti-symmetric output is one in which the two photons each exit opposite ports of the beam splitter. The $\sqrt{\text{SWAP}}$ operation is defined in Eq. (42), and may be performed with a Mach-Zehnder interferometer with a $\pi/2$ phase between the two interfering paths [11]. We chose a displaced Sagnac in place of a Mach-Zehnder interferometer for its improved phase stability. Using a Mach-Zehnder interferometer would require a system for phase stabilization to run for the duration of the measurements to maintain the $\pi/2$ phase, as this interferometer is highly sensitive to vibration. In a displaced Sagnac, this system is not necessary.

In the Mach-Zehnder configuration, the two beams each pass through one arm of the interferometer to be combined on a final beam splitter, as shown in Fig. 16-(B). In the displaced Sagnac configuration, each beam passes through the full interferometer, to be recombined on the first beam

splitter. This configuration is shown in Fig. 16-(A). One beam passes clockwise through the interferometer, and the other passes counter-clockwise through the interferometer. Because the photons in a Sagnac make a full pass through the interferometer, any change to one arm affects both the clockwise and counter-clockwise beams, and thus does not change the phase between them. This gives the Sagnac its characteristic phase stability.

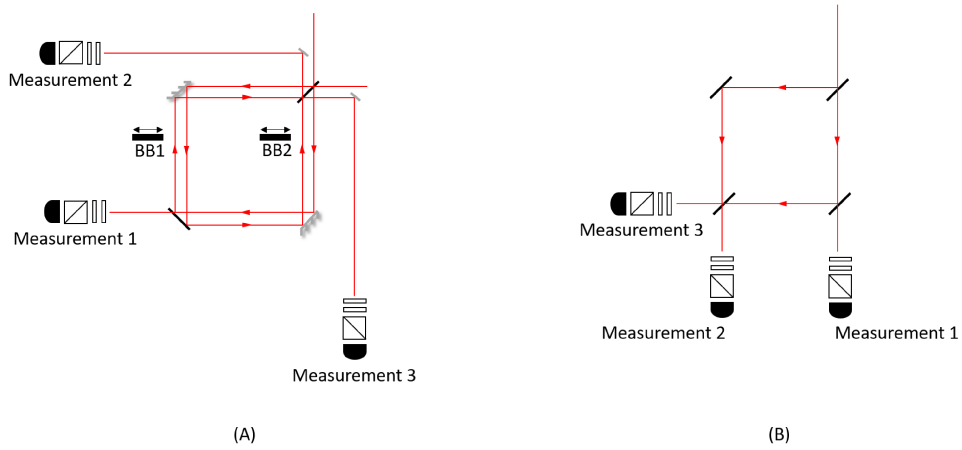


*Figure 16: Displaced Sagnac interferometer as compared to the same setup for a Mach-Zehnder interferometer. In the displaced Sagnac (A), the interfering beams pass either clockwise or counter-clockwise through the interferometer. Both beams pass through the first NPB twice, once on the way into the interferometer, and a second time when exiting the interferometer to measurement arms D1 and D2. This is equivalent to the Mach-Zehnder interferometer shown in (B), in which the interfering photons pass either through the right or left side of the interferometer and interfere on the fourth beamsplitter. The clockwise or counter-clockwise paths of the displaced Sagnac interferometer in (A) may be blocked by inserting beam blocks BB1 or BB2, respectively, as required to perform one of the four symmetry operations.*

In a typical Sagnac interferometer, the clockwise and counter-clockwise beams are perfectly aligned with the input beam(s). In a displaced Sagnac interferometer, the clockwise and counter-clockwise beams are parallel, but not overlapped. This allows the clockwise or counter-clockwise beams to be blocked, or unblocked, as required to perform the four symmetry operations described in Section 2.2.4.

When the counter-clockwise beam is blocked (BB2 inserted in Fig. 16-(A)), there will only be a coincidence at detectors D1 and D2 when the two photons both take the clockwise path through the interferometer. That is,

when the photons are projected onto the symmetric subspace and both exit the same port of the first beam splitter, BS1. The probability of jointly making measurements x at D1 and y at D2 is $P^{+1}(x, y)$ in Eq. (48).

When the clockwise beam is blocked (BB1 inserted in Fig. 16-(A)), there will only be a coincidence at detectors D1 and D2 when one photon takes the clockwise path to detector D1 and the other photon takes the counter-clockwise path to detector D2. That is, when the photons are projected onto the anti-symmetric subspace and exit opposite ports of the first beam splitter, BS1. The probability of jointly measuring x at D1 and y at D2 is $P^{-1}(x, y)$ in Eq. (48). The difference between these two probabilities, $P^{+1}(x, y)$ and $P^{-1}(x, y)$, gives the real part of the Dirac distribution D(x,y).

The $\sqrt{\text{SWAP}}$ operation, which is defined in Eq. (42), is performed when both arms of the interferometer are unblocked. The $\sqrt{\text{SWAP}}$ operation requires a $\pi/2$ phase between the clockwise and counter-clockwise paths. A Sagnac interferometer has a natural phase of $\pi$; photons entering one port of the first beam splitter (BS1) will necessarily exit the same port of the beam splitter at the output of the interferometer, i.e. they undergo a SWAP operation. To give a phase of $\pi/2$ between the two paths, the angle of the second beam splitter (BS2 in Fig. 16-(A)) was adjusted until the output intensities were equal at the output ports of BS1. This was tested using classical light, for which half the input power was expected at each output. A third measurement, D3, was also used to confirm the $\pi/2$ phase in the interferometer; for this phase, it is expected that there will be a drop in coincidences between D2 and D3 (the two detectors at the output ports of BS1 in Fig. 16-(A)). This can be understood by considering the Hong-Ou-Mandel effect; if the phase in the interferometer is $\pi/2$, then the interferometer acts as a beam splitter and we expect to see a similar effect as for the HOM dip, in which there is a drop in coincidences at the two beam splitter output ports.

When the phase of the interferometer is $\pi/2$, the symmetric and anti-symmetric outputs undergo a $\sqrt{\text{SWAP}}$ operation . For this interferometer configuration, the probability of measuring x at D1 and y at D2 is $P^{+i}(x, y)$ in Eq. (48).

To perform a $\sqrt{\text{SWAP}}$ with a phase of $-\pi/2$, the roles of the two detectors were reversed. That is, a measurement of x was performed at D2 and a measurement of y at D1. The probability of jointly measuring x at D2 and y at D1 in this configuration gives $P^{-i}(x, y)$.

These four interferometer configurations, then, allow for measurement of the four probabilities required to construct the Dirac distribution in Eq. (48). The method for determining the Dirac distribution and reconstruct

the density matrix of the target photon is discussed in Section 4.4.

Due to losses in the interferometer, the success probabilities for the four symmetry operators are as follows: 3/32 for $P^{+1}(x,y)$; 1/32 for $P^{-1}(x,y)$; and 1/8 for $P^{+i}(x,y)$ and $P^{-i}(x,y)$. For $P^{+1}(x,y)$, the probability of having the photons exit together in the clockwise arm of the interferometer is 3/8 (i.e. this is the success probability for producing optimal clones at BS1). There is then a 50% loss at the two beam splitters at D1 and D2, which reduces the success probability to 3/32. That is, the probability of having a photon at D1 and a photon at D2 when the counter-clockwise arm is blocked (BB2 in Fig. 16-(A)). For $P^{-1}(x,y)$, the probability of having the two photons exit opposite ports of BS1 is 1/4. Here, the photons pass through both arms of the interferometer, so there are 50% losses at BS2, BS3, and BS4. The success probability then reduces to 1/32. $P^{+i}(x,y)$ and $P^{-i}(x,y)$ combine these two cases, so the success probability is 3/32 + 1/32 = 1/8.

### 4.3.1 Tests of Interferometer Phase

The phase of the Sagnac interferometer must be $\pi/2$ to perform the $\sqrt{\text{SWAP}}$ operation. This interferometer phase was achieved by adjusting the alignment of beam splitter BS2, which controls the overlap of the clockwise and counter-clockwise beams on BS1. When the phase of the interferometer is $\pi/2$, the full interferometer acts as a 50/50 beam splitter. This allows the interferometer phase to be tested in two ways. First, by observing a Hong-Ou-Mandel dip at the output of the interferometer; as the interferometer acts as a beam splitter, the same Hong-Ou-Mandel interference should be observed at the output of the interferometer (at detectors D2 and D3). A scan of this dip was performed at detectors D2 and D3, with results shown in Fig. 17.

The visibility of this dip, as calculated from Eq. (71), was 84%. The central dip position is different from the central dip position in Fig. 15. This was due to the rotating wave plate placed at the output of fiber F2, which changed the optical path length of this arm into the beam splitter. This was the rotating wave plate used to prepare the mixed state entering the cloning beam splitter.

To test that the interferometer was indeed performing a $\sqrt{\text{SWAP}}$ operation, the input state was set to $|V_1 H_2\rangle$, where 1 and 2 represent the inputs at fibers F1 and F2, respectively. For this input state, a $\sqrt{\text{SWAP}}$ operation will produce output state $|V_2 H_3\rangle - i\,|H_2 V_3\rangle$ (where 2 and 3 represent the outputs at detectors D2 and D3, respectively. To confirm that the interfer-

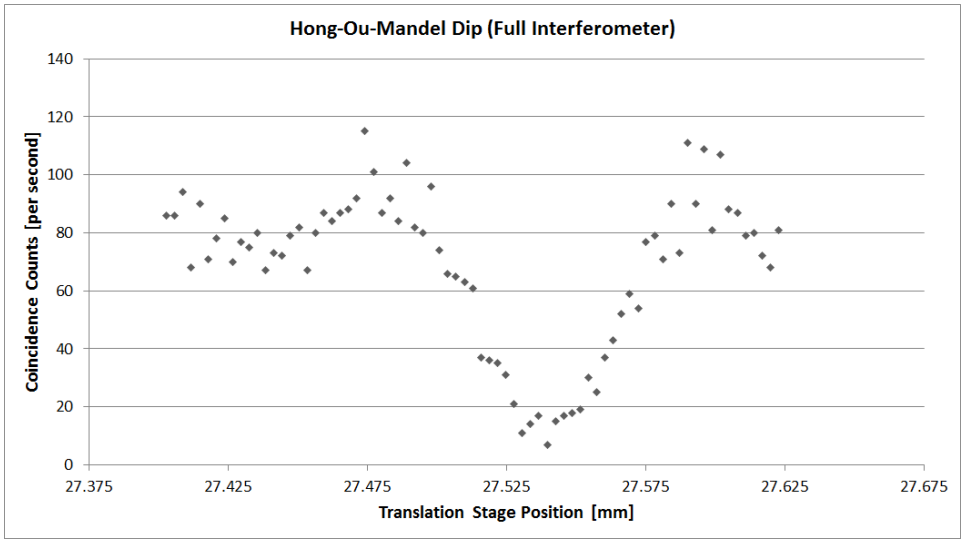


*Figure 17: Hong-Ou-Mandel dip for the full displaced Sagnac interferometer.*

ometer is performing a $\sqrt{\text{SWAP}}$ operation, the two-photon state at detectors D2 and D3 can be determined through QST to confirm that this state has high fidelity with the state $|V_2H_3\rangle - i\,|H_2V_3\rangle$.

The density matrix describing this state is as follows:

$$\rho_{\sqrt{\text{SWAP}}\ theory} = \begin{bmatrix} 0 & 0 & 0 & 0 \\ 0 & 1/2 & -i/2 & 0 \\ 0 & i/2 & 1/2 & 0 \\ 0 & 0 & 0 & 0 \end{bmatrix}. \tag{72}$$

The following two-photon state was reproduced through 16-measurement QST performed at detectors D2 and D3:

$$\rho_{\sqrt{\text{SWAP}}\ exp} = \begin{bmatrix} 0.028 & 0.068 - 0.002i & -0.014 - 0.040i & 0.008 - 0.011i \\ 0.06 + 0.002i & 0.509 & 0.238 - 0.115i & -0.003 - 0.019i \\ -0.014 + 0.040i & -0.238 + 0.115i & 0.419 & -0.031 - 0.019i \\ 0.008 + 0.011i & -0.003 - 0.059i & -0.031 + 0.019i & 0.044 \end{bmatrix}. \tag{73}$$

This density matrix is shown below in Fig. 18.

The trace distance between $\rho_{\sqrt{\text{SWAP}}\ exp}$ and $\rho_{\sqrt{\text{SWAP}}\ theory}$ is 0.2546.

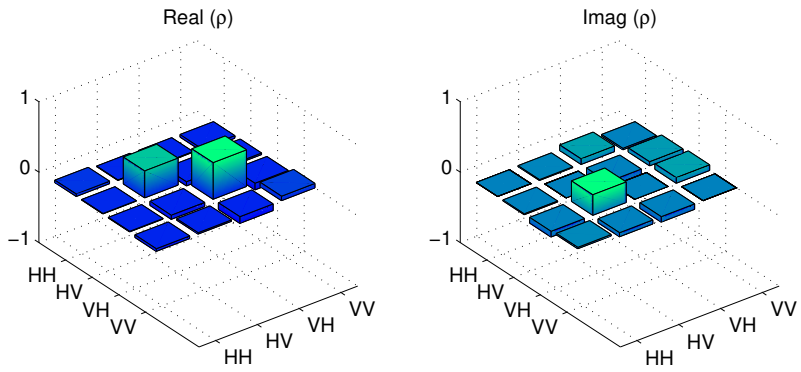


*Figure 18: Real and imaginary parts of the density matrix for a square root SWAP operation performed on input state $|V_a H_b\rangle$.*

## 4.4 Quantum State Tomography

After passing through the interferometer, the two photons exited the output ports of the cloning beam splitter (BS1 in Fig.16-(A)). Due to the nature of the displaced Sagnac interferometer, the photons exiting the first beam splitter are parallel to, but not collinear with, the incoming photons. The displacement between beams in the interferometer was 4 mm, which allowed outgoing photons to be redirected using D-mirrors placed at the two outputs of BS1.

The two photons were collected using fiber-coupled avalanche photodiodes (APDs). A half-wave plate, quarter-wave plate, and polarizing beam splitter placed before each APD allowed for quantum state tomography to be performed to measure the two-photon state. Quantum state tomography is a method that allows us to estimate the state of a system from the results of measurements of a set of observables. We perform these measurements on multiple copies of the same system. To determine the two-photon state of photon pairs exiting the Sagnac interferometer, we performed 16 measurements, all combinations of projections nto $|H\rangle$, $|V\rangle$, $|D\rangle$, and $|R\rangle$. For each of these 16 combinations, we measure the coincidences between these two

detectors (detectors D2 and D3, for tests of the $\sqrt{\text{SWAP}}$, and detectors D1 and D2, for measurements of the two-photon state of the optimal quantum clones). The two-photon state was reconstructed from these measurements using a tomography interface operated by the Kwiat Quantum Information Group. Reconstructing the state in this manner allows us to confirm that the cloning device is producing optimal quantum clones that have high fidelity with the predicted two-photon state.

The HWP and QWP were mounted in rotating stages to allow for full automation of the quantum state tomography measurements. The method by which these wave plates were aligned is given in Appendix .

Quantum state tomography was automated using a Labview code that controlled the QWP and HWP motors, the translation stage at fiber F1, and the coincidence counter. Sixteen measurements were performed for all combinations of polarization states $|H\rangle$, $|V\rangle$, $|D\rangle$, and $|R\rangle$ at detectors D1 and D2.

# 5 Direct Measurement of the Target Photon Polarization State

To reconstruct the density matrix describing the state of the target photon, we performed four measurements for each of the interferometer configurations described in Section 4.3.

Recall that the Dirac distribution can be determined using Eq. (48):

$$D(x,y) = \frac{d+1}{2}\left[P^{+1}(x,y) - P^{-1}(x,y) - i\left(P^{+i}(x,y) - P^{-i}(x,y)\right)\right].$$

We measured in the H/V basis at detector D1 and in the D/A basis at detector D2. There are then four measurement combinations: a measurement of H at D1 and D at D2; a measurement of H at D1 and A at D2; a measurement of V at D1 and D at D2; and a measurement of V at D1 and A at D2. We measured the coincidences between detectors D1 and D2 for each of these measurement combinations.

When we measured H and D for each of the four symmetry operations discussed in Section 4.3 (BB1 inserted; BB2 inserted; both beam blocks removed; and both beam blocks removed with the measurement order reversed), we obtain the four probabilities in Eq. 48 and can determine the real and imaginary parts of D(H,D). By repeating these measurements for the other three measurement combinations, we can fully determine the real and imaginary parts of the Dirac distribution.

The density matrix of the target photon was reconstructed using a method proposed by Lundeen and Bamber in [3]. Taking the Dirac Distribution, D, each term in the density matrix can be calculated using Eq. (74):

$$\rho_{m,n} = \sum_{k=0}^{N-1} D_{m,k} \exp\left(\frac{2\pi i}{N}(m-k)n\right), \tag{74}$$

where $\rho_{m,n}$ is the value in the $m^{th}$ row and $n^{th}$ column of density matrix $\rho$, $D_{m,k}$ is the value in the $m^{th}$ row and $k^{th}$ column of the Dirac Distribution D, and N is the dimension of the Hilbert space. This is a stepwise Fourier transform, which is used to reconstruct the density matrix from Dirac Distribution D as the H/V and D/A bases are mutually unbiased Fourier bases.

More simply, the density matrix $\rho$ can be reconstructed from Dirac Distribution D as follows:

$$\rho = \begin{bmatrix} D_{0,0} + D_{0,1} & D_{0,0} - D_{0,1} \\ D_{1,0} - D_{1,1} & D_{1,0} + D_{1,1} \end{bmatrix}. \tag{75}$$

The reconstructed density matrix could then be compared the expected density matrix for the target state using a measure known as trace distance, which is discussed in the following section.

## 5.1 Fidelity and Trace Distance

We will use two measures to quantify how closely our results match with theory. The first of these two measures is the fidelity, which gives a measure of the 'closeness' of two states. For pure states, fidelity gives a measure of the overlap between the two states. Since we are not dealing only with pure states (the cloned state, for example, is a mixed state), we will use a generalization of the fidelity calculation that applies to mixed states. For two states, given by $\rho_{\text{exp}}$ and $\rho_{\text{theory}}$, the fidelity between these two states is:

$$F(\rho_{\text{exp}}, \rho_{mathrmtheory}) = Tr\left[\sqrt{\sqrt{\rho_{\text{exp}}}\rho_{\text{theory}}\sqrt{\rho_{\text{exp}}}}\right]. \tag{76}$$

For two orthogonal states, the fidelity will be 0, and for two identical states, the fidelity will be 1.

The second measure we will use is the trace distance. Trace distance gives a measure of the distinguishability between two quantum states. The average probability of distinguishing two quantum states, $\rho_{\text{exp}}$ an $\rho_{\text{theory}}$, by

measurement is $1/2 + 1/2\mathrm{T}(\rho_{\mathrm{exp}}, \rho_{\mathrm{theory}})$, where the trace distance $\mathrm{T}(\rho_{\mathrm{exp}}, \rho_{\mathrm{theory}})$ is given by:

$$T(\rho_{\mathrm{exp}}, \rho_{\mathrm{theory}}) = \frac{1}{2}\mathrm{Tr}|\rho_{\mathrm{exp}} - \rho_{\mathrm{theory}}| \tag{77}$$

$$= \frac{1}{2}\mathrm{Tr}\left[\sqrt{(\rho_{\mathrm{theory}} - \rho_{\mathrm{exp}})^{\dagger}(\rho_{\mathrm{theory}} - \rho_{\mathrm{exp}})}\right]. \tag{78}$$

The factor of $1/2$ limits the results to be between 0 and 1, where 0 indicates that the two states are indistinguishable.

Fidelity and trace distance are related by the following inequality:

$$1 - F(\rho_{\mathrm{exp}}, \rho_{\mathrm{theory}}) \leq T(\rho_{\mathrm{exp}}, \rho_{\mathrm{theory}}), \tag{79}$$

The trace distance can then give a lower limit on fidelity (e.g. a trace distance of 0.1 would imply that the fidelity is at least 0.9).

Because a theoretical limit has been placed on the fidelity of optimal quantum clones, the fidelity is a convenient measure to confirm that the quantum clones produced in this experiment are indeed optimal. However, we use the trace distance as a measure of how closely the reconstructed density matrix for target state $\rho_{\mathrm{target}}$ matches the expected density matrix for this state. The reconstructed density matrix may not be Hermitian, in part due to the statistical errors in the counts during our coincidence measurements, but also due to the fact that the components of the Dirac distribution are measured individually. While the density matrices obtained by performing quantum state tomography are constrained to be Hermitian, these constraints are not imposed with when reconstructing the density matrix using our measurement technique. In this case the fidelity may return a complex result, and thus trace distance can provide a more meaningful measure of the closeness of the two states.

## 5.2 Production of Optimal Quantum Clones

The cloning device was tested for three target states, these being $|H\rangle$, $|V\rangle$, and $|A\rangle$.

Optimal quantum clones were produced by sending one of these target states into one port of the non-polarizing beam splitter (BS1 in Fig. 16-(A)), and a mixed state into the other port of the beam splitter. The target states were produced by adjusting the angles of a quarter- and half-wave plate placed at the output of fiber F1. The mixed state was produced by a half-wave plate placed in a motorized rotation mount. This half-wave plate

was set to rotate for the duration of the measurement, so the second photon had no set polarization over each measurement.

The state of the optimal quantum clones was measured at detectors D1 and D2 when the two photons exited the same port of the beam splitter (BB1 inserted in Fig. 16-(A)). The two-photon density matrix was determined using quantum state tomography. We performed 16 measurements (all combinations of polarization states $|H\rangle$, $|V\rangle$, $|D\rangle$, and $|R\rangle$).

The results of quantum state tomography, and comparisons to the predicted two-photon density matrices, are given for target states $|H\rangle$, $|V\rangle$, and $|A\rangle$ in the following three sections.

### 5.2.1 Optimal Quantum Clones of Target State $|H\rangle$

For target state $|H\rangle$, and for the following two target states, the two-photon polarization state at the output of the cloning beam splitter was determined through quantum state tomography (QST), performed over sixteen measurements (all combinations of $|H\rangle$, $|V\rangle$, $|D\rangle$, and $|R\rangle$). For each measurement, coincidence counts between the two detectors were measured over 5 minutes.

For input state $|H\rangle$, the expected output state for the optimally cloned photons was as follows:

$$\rho_{Htheory} = \frac{2}{3}(\Pi^{+}_{cd}\rho_H \otimes \Pi^{+}_{cd}) \qquad = \begin{bmatrix} 2/3 & 0 & 0 & 0 \\ 0 & 1/6 & 1/6 & 0 \\ 0 & 1/6 & 1/6 & 0 \\ 0 & 0 & 0 & 0 \end{bmatrix}. \qquad (80)$$

The results of QST, measured at detectors D1 and D2, was as follows:

$$\rho_{Hexp} = \begin{bmatrix} 0.532 & -0.058+0.016i & 0.015-0.024i & -0.005-0.025i \\ -0.058-0.016i & 0.205 & -0.007+0.012i & -0.022i \\ 0.015+0.024i & -0.007-0.012i & 0.243 & -0.043+0.011i \\ -0.005+0.025i & 0.022i & -0.043-0.011i & 0.020 \end{bmatrix}. \qquad (81)$$

The theoretical and experimental density matrices for the clones of a horizontally polarized photon are shown below in Fig. 19.

For clones of $|H\rangle$, the fidelity of $\rho_{exp}$ with the expected output state, $\rho_{CD}$ was 0.86. Ideally, we would like a higher fidelity with respect to the predicted state for these optimal quantum clones. This lower fidelity may be due to the reduced off-diagonal terms in $\rho_{\mathrm{H\ exp}}$. We believe that this

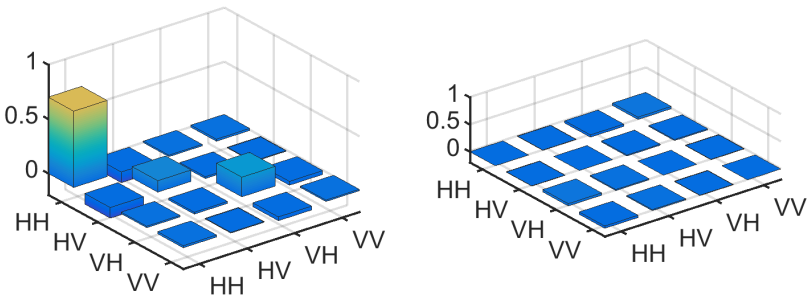


*Figure 19: Real and imaginary parts of the experimentally measured density matrix for a target state with polarization H*

is caused by a birefringent phase introduced by the beam splitters in the displaced Sagnac interferometer. Though the clones of $|H\rangle$ are still shown to be close to optimal (see below), this birefringent phase has a greater effect on the other two tested states, $|V\rangle$ and $|A\rangle$, so this birefringent phase may need to be compensated for in the interferometer to improve these results.

To confirm that these clones are optimal, we take a partial trace over this two photon state to determine the state of each of the quantum clones. Comparing the state of each photon with the target state $\rho_{\text{target}}$, we find that one clone has a fidelity of 0.82 with the target state, and the other clone has a fidelity of 0.87. Though the theoretical limit is 5/6, or 0.83, the higher fidelity for one of the clones may be due to statistical counting errors, which may account for a 5% error in the QST measurements.

### 5.2.2 Optimal Quantum Clones of Target State $|V\rangle$

For input state $|V\rangle$, the expected output state for the optimally cloned photons was:

$$\rho_{V theory} = \frac{2}{3}(\Pi^{+}_{cd}\rho_V \otimes \Pi^{+}_{cd}) \qquad = \begin{bmatrix} 0 & 0 & 0 & 0 \\ 0 & 1/6 & 1/6 & 0 \\ 0 & 1/6 & 1/6 & 0 \\ 0 & 0 & 0 & 2/3 \end{bmatrix}. \tag{82}$$

The two-photon polarization density matrix, measured at detectors D1 and D2, was as follows:

$$\rho_{V exp} = \begin{bmatrix} 0.021 & 0.027 - 0.007i & -0.004 - 0.012i & -0.065 - 0.055i \\ 0.027 + 0.007i & 0.176 & 0.073 - 0.076i & -0.023 + 0.073i \\ -0.004 + 0.012i & 0.073 + 0.076i & 0.0205 & 0.058 + 0.089i \\ -0.065 + 0.055i & -0.023 - 0.073i & 0.058 - 0.089i & 0.598 \end{bmatrix}. \tag{83}$$

The fidelity of $\rho_{V exp}$ with the predicted state, $\rho_{V theory}$ is 0.92. The optimal quantum clones of input state $|V\rangle$ have higher fidelity with respect to the predicted state than for input state $|H\rangle$. Ideally, we would like to be able to produce optimal clones of any input state with the same fidelity; in future work, we would like to improve the fidelity of these cloned states with respect to the expected cloned state.

Taking a partial trace to determine the state of each of these cloned photons, the fidelity of each photon with respect to the target state is 0.68 and 0.76. Both fidelities are lower than 0.83, which implies that these clones are not optimal. It is possible that some of this reduction is due to the birefringent phase in the interferometer.

The theoretical and experimental density matrices for the clones of a vertically polarized photon are shown below in Figs. 20 and 21, respectively.

### 5.2.3 Optimal Quantum Clones of Target State $|A\rangle$

For input state $|A\rangle = \frac{1}{\sqrt{2}}(H - V))$, the expected output state is:

$$\rho_{A\ theory} = \begin{bmatrix} 1/3 & -1/6 & -1/6 & 0 \\ -1/6 & 1/6 & 1/6 & -1/6 \\ -1/6 & 1/6 & 1/6 & -1/6 \\ 0 & -1/6 & -1/6 & 1/3 \end{bmatrix}. \tag{84}$$

The two-photon polarization state, reconstructed from QST at detectors D1 and D2, was as follows:

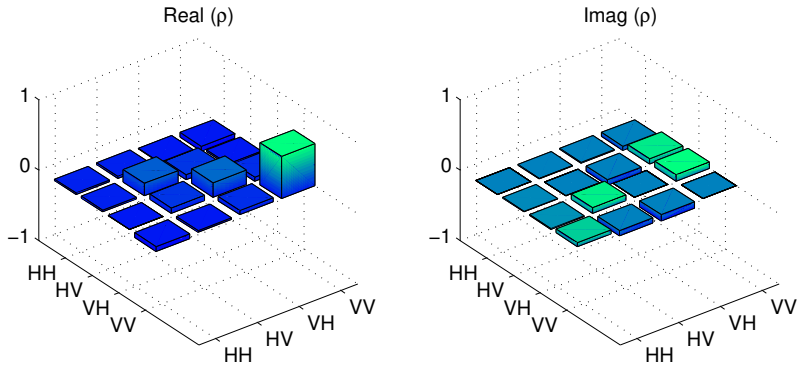


*Figure 20: Real and imaginary parts of the theoretically calculated density matrix for a target state with polarization V*

$$\rho_{A\ exp} = \begin{bmatrix} 0.204 & 0.114 + 0.033i & -0.005 - 0.128i & -0.004 - 0.004i \\ -0.114 - 0.033i & 0.252 & -0.004 + 0.015i & -0.005 - 0.095i \\ -0.005 + 0.128i & -0.004 - 0.015i & 0.263 & -0.104 + 0.023i \\ -0.004 + 0.004i & -0.005 + 0.095i & -0.104 - 0.023i & 0.2810 \end{bmatrix}. \tag{85}$$

The fidelity of $\rho_{exp}$ with $\rho_{Atheory}$ is 0.77. After taking a partial trace of the two-photon state, the fidelities of each clone with respect to the target state were found to be 0.43 and 0.81. The reduced fidelity for the two-photon state, as well as the unequal fidelities of the two clones, is likely due to the birefringent phase in the interferometer. The inequality between the two fidelities may occur because one photon exits halfway through the interferometer, while the second cloned photon passes through one final beam splitter (BS4) prior to measurement. This effect may be especially pronounced for target state $|A\rangle$ because it is a combination of $|H\rangle$ and $|V\rangle$; a birefringent phase between the horizontally and vertically polarized components would then affect the output for target state $|A\rangle$ more than either target state $|H\rangle$ or $|V\rangle$.

The theoretical and experimental density matrices for the clones of an

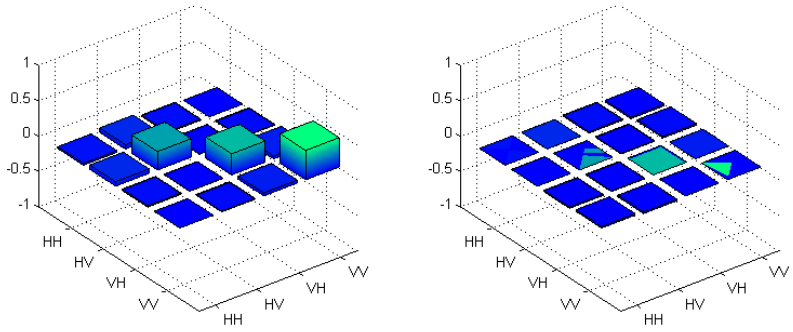


*Figure 21: Real and imaginary parts of the experimentally measured density matrix for a target state with polarization $|V\rangle$*

anti-diagonally polarized photon are shown below in Figs. 22 and 23, respectively.

### 5.3 Joint Measurement

To reconstruct the real and imaginary parts of the target state density matrix, four measurements were made at detectors D1 and D2, those being all combinations of $|H\rangle$ or $|V\rangle$ at D1, and $|A\rangle$ or $|D\rangle$ at D2. For the real part of the joint measurement, these measurements were performed with beam block BB1 inserted (i.e. measuring only the symmetric, or successful, cloning output), and again with beam block BB2 inserted (i.e. measuring only the anti-symmetric output). For the imaginary part of the joint measurement, the beam block was removed and the same four measurements were taken at D1 and D2 (i.e. a phase of $\pi/2$ between the two interferometer arms), and finally the . These measurements were made for three target states: $|H\rangle$, $|V\rangle$, and $|A\rangle$. The real and imaginary parts of the Dirac distribution were calculated from these measurements, and a density matrix for the input state was then reconstructed from the Dirac distribution. The fidelities of the Dirac distribution and density matrix were then calculated with respect

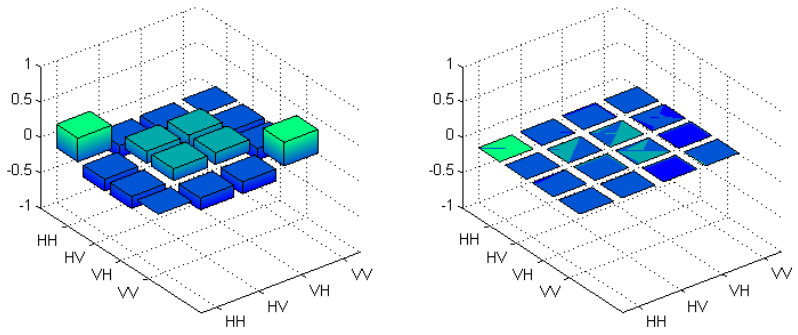


*Figure 22: Real and imaginary parts of the theoretically calculated density matrix for target state with polarization A*

to the theoretical Dirac distribution and density matrix, respectively. These results are summarized in the following sections.

### 5.3.1 Reconstruction of the Density Matrix of Target State $|H\rangle$

The density matrix describing input state $|H\rangle$ is:

$$\rho_H = \begin{bmatrix} 1 & 0 \\ 0 & 0 \end{bmatrix}. \tag{86}$$

This is the density matrix we aim to reconstruct from the joint measurements on the optimal clones of target state $|H\rangle$. To reconstruct this density matrix, the Dirac distribution was first calculated from the four measurement outcomes at D1 and D2.

To determine the Dirac distribution, a set of four measurements were made for each of four interferometer configurations. The same four measurements were made for each interferometer configuration, those being a measurement of H or V at detector D1 and a measurement of D or A at detector D2. For the real part of the Dirac distribution, these measurements

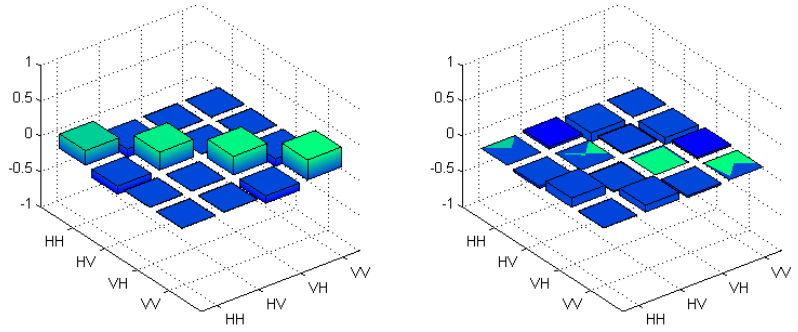


*Figure 23: Real and imaginary parts of the experimentally measured density matrix for a target state of A*

were made with each interferometer arm blocked, first the clockwise beam (beam block BB2 inserted) and second with the counter-clockwise beam (beam block BB1 inserted). These measurements correspond to the terms $P^{+1}(x, y)$ and $P^{-1}(x, y)$ in Eq. (56). For the imaginary part of the Dirac distribution, these measurements were made with both interferometer arms open, once with a phase of $\pi/2$, and second with a phase of $-\pi/2$ (i.e. a swap of the roles of D2 and D3). These measurements respond to $P^{+i}(x, y)$ and $P^{-i}(x, y)$ in Eq. (56).

The real part of the Dirac distribution is as follows:

| | Theory | Experiment |
|---|---|---|
| D(H,D) | 0.5 | 0.434 |
| D(H,A) | 0.5 | 0.542 |
| H(V,D) | 0 | 0.018 |
| H(V,A) | 0 | 0.027 |

The imaginary part of the Dirac distribution is as follows:

**Dirac Distribution for Target State $|H\rangle$**

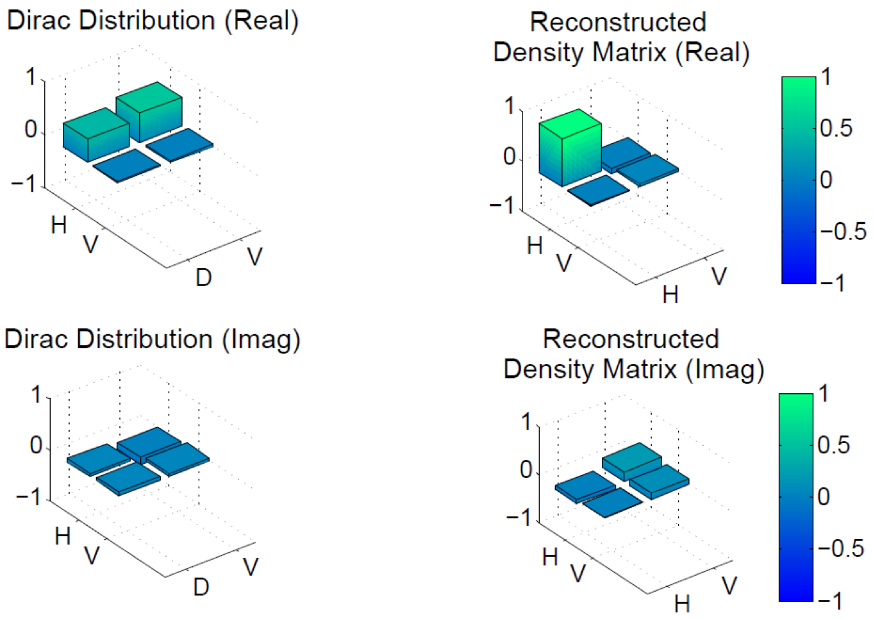


*Figure 24: Real and imaginary parts of the Dirac distribution (left) and reconstructed density matrix (right) for target state $|H\rangle$.*

| | Theory | Experiment |
|---|---|---|
| D(H,D) | 0 | 0.052 |
| D(H,A) | 0 | -0.147 |
| D(V,D) | 0 | 0.059 |
| D(V,A) | 0 | 0.057 |

The density matrix describing the polarization state of the target photon was reconstructed from the Dirac distribution using Eq. (75). The Dirac distribution and reconstructed density matrix for the target photon are shown in Fig. 24.

Using Eq.(78) trace distance between this reconstructed density matrix and $\rho_H$ was found to be 0.1367.

### 5.3.2 Reconstruction of the Density Matrix of Target State $|R\rangle$

For input state R = $(|H\rangle + i\,|V\rangle)/\sqrt{2}$, the density matrix describing this state is:

$$\rho_R = \begin{bmatrix} 1/2 & -i/2 \\ i/2 & 1/2 \end{bmatrix}. \tag{87}$$

The real part of the Dirac distribution is as follows:

| | Theory | Experiment |
|---|---|---|
| D(H,D) | 0.25 | 0.287 |
| D(H,A) | 0.25 | 0.237 |
| H(V,D) | 0.25 | 0.188 |
| H(V,A) | 0.25 | 0.128 |

The imaginary part of the Dirac distribution is as follows:

| | Theory | Experiment |
|---|---|---|
| D(H,D) | -0.25 | -0.1 |
| D(H,A) | 0.25 | 0.193 |
| D(V,D) | 0.25 | 0.165 |
| D(V,A) | -0.25 | -0.251 |

The density matrix of the target photon was reconstructed from this Dirac distribution using Eq. (74). The Dirac distribution and reconstructed density matrix for this target state are shown in Fig. 25.

From Eq. (78), the trace distance between the reconstructed density matrix and $\rho_R$ is 0.1548.

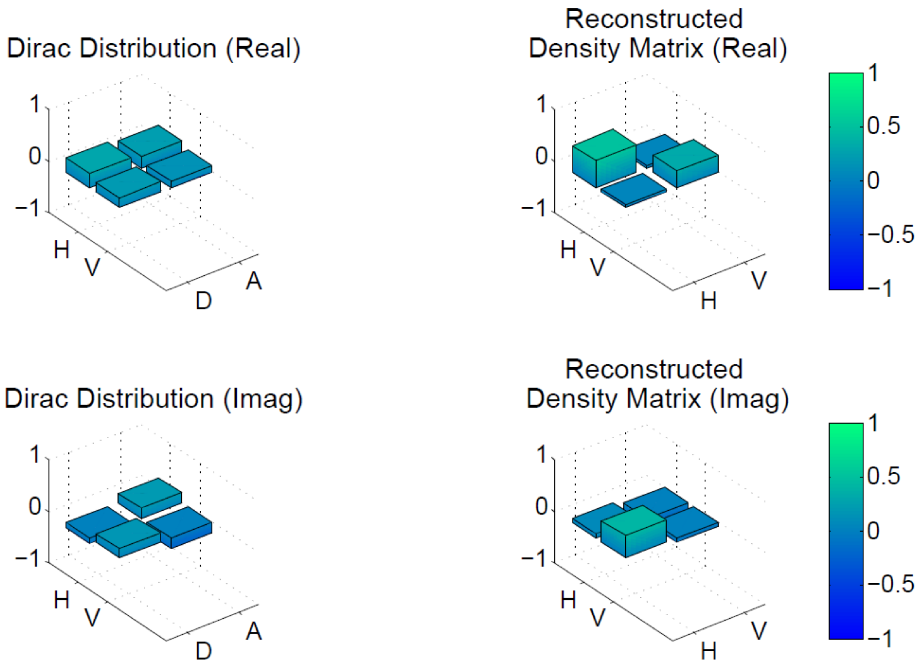


*Figure 25: Real and imaginary parts of the Dirac distribution (left) and reconstructed density matrix (right) for target state* $|R\rangle$.

# 6 Conclusion

The purpose of this section was to demonstrate the experiment proposed by Hofmann, who showed that weak values appear in joint measurements performed on optimal quantum clones.

These optimal quantum clones were produced on a non-polarizing beam splitter by sending in a target state and maximally mixed state into opposite ports of the beam splitter. This cloning device was tested for input states $|H\rangle$, $|V\rangle$, and $|A\rangle$. The trace distance was used as a measure of how indistinguishable these states are from the expected cloned states as predicted by theory.

To measure the real part of the Dirac distribution, two measurements were performed in the H/V and D/A bases, first on the symmetric output of the beam splitter (when both photons exit the same beam splitter port), and then on the anti-symmetric beam splitter output (when both photons exit opposite beam splitter ports. The imaginary part of the Dirac distribution was determined from the same two measurements when the two outcomes (symmetric and anti-symmetric) were interfered in a displaced Sagnac with a phase of $\pi/2$, and with a phase of $-\pi/2$. These measurements were performed on optimal clones of states $|H\rangle$ and $|R\rangle$, and the density matrices of these target states were reconstructed from the four polarization measurements.

Trace distance was used as a measure of how distinguishable these reconstructed density matrices were from the density matrices describing the target state. The trace distances for input states $|H\rangle$ and $|R\rangle$ were 0.1367 and 0.1548, respectively. Though we have not perfectly reproduced the density matrices of the input states, this method shows promise as a means of directly measuring the state of quantum systems. In future work, we aim to improve the fidelity of clones produced at the non-polarizing beam splitter, and to eliminate the birefringent phase in the interferometer to allow improved results for additional polarization states.

These results confirm that the weak measurement result appears in correlations between optimal quantum clones, as proposed by Hofmann, and that this measurement technique may be used to directly measure quantum states. Though this measurement technique is very different from the weak measurement technique, both approaches yield the same result, which speaks to the universality of joint measurements.

## References


[1] D. T. Smithey, M. Beck, M. G. Raymer, and A. Faridani, "Measurement of the wigner distribution and the density matrix of a light mode using optical homodyne tomography: Application to squeezed states and the vacuum," *Phys. Rev. Lett.*, vol. 70, pp. 1244–1247, 9 Mar. 1993.

[2] Y. Aharonov, D. Z. Albert, and L. Vaidman, "How the result of a measurement of a component of the spin of a spin-1/2 particle can turn out to be 100," *Phys. Rev. Lett.*, vol. 60, pp. 1351–1354, 14 Apr. 1988.

[3] J. S. Lundeen, B. Sutherland, A. Patel, C. Stewart, and C. Bamber, "Direct measurement of the quantum wavefunction," *Nature*, vol. 474, no. 7350, pp. 188–191, Jun. 2011, ISSN: 0028-0836.

[4] H. F. Hofmann, "How weak values emerge in joint measurements on cloned quantum systems," *Phys. Rev. Lett.*, vol. 109, p. 020 408, 2 Jul. 2012.

[5] J. Z. Salvail, M. Agnew, A. S. Johnson, E. Bolduc, J. Leach, and R. W. Boyd, "Full characterization of polarization states of light via direct measurement," *Nat Photon*, vol. 7, no. 4, pp. 316–321, Apr. 2013, ISSN: 1749-4885.

[6] W. K. Wootters and W. H. Zurek, "A single quantum cannot be cloned," *Nature*, vol. 299, no. 5886, pp. 802–803, Oct. 1982.

[7] N. Gisin and S. Massar, "Optimal quantum cloning machines," *Physical review letters*, vol. 79, no. 11, p. 2153, 1997.

[8] G. M. D'Ariano, C. Macchiavello, and M. F. Sacchi, "Joint measurements via quantum cloning," *Journal of Optics B: Quantum and Semiclassical Optics*, vol. 3, no. 2, p. 44, 2001.

[9] W. T. Irvine, A. L. Linares, M. J. de Dood, and D. Bouwmeester, "Optimal quantum cloning on a beam splitter," *Physical review letters*, vol. 92, no. 4, p. 047 902, 2004.

[10] D. Bruss, A. Ekert, and C. Macchiavello, "Optimal universal quantum cloning and state estimation," *Physical review letters*, vol. 81, no. 12, p. 2598, 1998.

[11] A. Cernoch, J. Soubusta, L. Bartuskova, M. Dusek, and J. Fiurasek, "Experimental realization of linear-optical partial swap gates," *Physical Review Letters*, vol. 100, no. 18, p. 180 501, May 2008.

[12] J. S. Lundeen and C. Bamber, "Procedure for direct measurement of general quantum states using weak measurement," *Physical review letters*, vol. 108, no. 7, p. 070 402, 2012.

# Appendix C Details of Experimental Components and Part Numbers

This section gives details of part numbers and specifications for the elements of the experimental setup described in Section 4.

The high-pass and low-pass filters used to filter the pump beam before and after down-conversion were purchased from Thorlabs. The long-pass filter had a cut-off frequency of 700 nm (part number FELH0700) and the short-pass filter had a cut-off frequency of 450 nm (part number FESH0450).

The fiber-coupled APDs used in this experiment were manufactured by Exceitas (part number SPCM-AQRH-FC). These photon counting modules are operated above threshold, so a single photon arriving at the detector is counted as an electronic pulse at the output. These counters have a peak detection efficiency of 55% at 830 nm, though there may be some slight additional losses due to the fiber coupling, and a dark count rate of 100/s.

# Appendix D Half- and Quarter-Wave Plate Alignment

This method was used to align the half- and quarter-wave plates used in the measurements described in Sections 4.4 and 5.

The axis of each half-wave plate was determined by placing the half-wave plate in front of a PBS and observing the output on a photodiode as the half-wave plate was rotated. When passing through the full 360° range, there are four peaks, representing the angles for which horizontally polarized light is maximally transmitted through the beam splitter (i.e the half-wave plate is aligned to transmit $|H\rangle$). The angle corresponding to the peak with the maximum intensity was chosen as the axis for transmission of $|H\rangle$ for the quantum state tomography.

The axes of the quarter-wave plates were determined by the same method. To confirm the axes as determined by this method, the quarter-wave plate was set to transmit at 45°, and a half-wave plate was placed after the quarter-wave plate. For this angle of transmission, there should be no change in the intensity of the transmitted light when the half-wave plate was rotated

through its full 360° range.

# Appendix E Alignment into Polarization Maintaining Fibers

This method was used to align the polarization of single photons entering the polarization maintaining (PM) fibers, as described in Section 4.1.

For this alignment, a half-wave plate was placed in front of the PM fiber and a PBS was placed at the output of the PM fiber. The HWP was aligned until the intensity of light reflected at the PBS was minimized. The fiber was then slightly stressed by heating, and if there was an increase in the reflected intensity, then HWP was rotated to minimize the reflected intensity. This process was repeated until the reflected intensity was unchanged when the fiber was stressed. When the fiber is properly aligned along the fiber axis, there should be no change to the output when the fiber is stressed.